Sanela Alibegic, BSc

01331265

Synthesis of thiophene- and tetraphenylethylene-linked Perylenemonoimides as Acceptor Materials and Investigation towards Photovoltaic Properties

MASTER THESIS

In partial fulfillment of the requirements for the academic degree

Diplom-Ingenieur

in the field of study of Technical Chemistry

submitted at

Graz University of Technology

Under the supervision of

Univ.-Prof. Dipl.-Ing. Dr.techn. Gregor Trimmel

Institute for Chemistry and Technology of Materials

Graz, February 2020

Affidavit / Eidesstattliche Erklärung

I declare that I have authored this thesis independently, that I have not used other than the declared sources/resources, and that I have explicitly indicated all material which has been quoted either literally or by content from the sources used. The text document uploaded to TUGRAZonline is identical to the present master’s thesis.

Ich erkläre an Eides statt, dass ich die vorliegende Arbeit selbstständig verfasst, andere als die angegebenen Quellen/Hilfsmittel nicht benutzt, und die in den benutzten Quellen wörtlich und inhaltlich entnommenen Stellen als solche kenntlich gemacht habe. Das in TUGRAZonline hochgeladene Textdokument ist mit der vorliegenden Masterarbeit identisch.

Date/Datum

Signature/Unterschrift

And those who were seen dancing were thought to be insane
by those who could not hear the music.
-- *Nietzsche*

Abstract

Fossil fuels have a great negative impact on the environment and are responsible for the greenhouse gas emission, resulting in global warming and climate changes. The concerns increased dramatically and therefore many scientists have attracted their attention towards alternative energy sources, which are environmentally friendly. Besides hydropower, wind power and biomass, photovoltaic technology is one of the most promising, since the sun can provide a nearly infinite amount of energy. Thus, silicon-based solar cells have developed and are commercially available on the market. In contrast to silicon based solar cells, organic solar cells (OSCs), comprising of polymers or small molecules, exhibit high flexibility, light weight, wide tunability, and easier production and research in this field is recently ongoing. The OSCs consist of an active layer, which comprises two semiconducting materials, a so-called (electron) donor and an acceptor material. The aim of this work was to synthesize acceptor materials, consisting of perylene monoimides (PMIs) coupled with different linker-units. The synthesis was accomplished via the Suzuki cross-coupling reaction, leading to bis- and quadrupole-coupled perylene monoimide moieties. Thiophene, hexylthiophene and tetraphenyle-based linkers were used, and the three synthesized products were characterized by ^{1}H-NMR spectroscopy and mass spectrometry and investigated towards optical properties. However, the thiophene compound exhibits solubility issues and the quadrupole-linked tetraphenyle product posed challenges concerning purification. Since the hexyl-thiophene compound (PMI-hT-PMI) had properties like good solubility, appropriate absorption range and suitable energy levels related to the donor material, it fulfilled the requirements as an acceptor material and solar cells comprising of PMI-hT-PMI and a conjugated polymer as donor (PBDB-T) were assembled. The OSCs were investigated towards donor/acceptor ratio and annealing temperatures. The devices reached promising power conversion efficiencies of 3.35% with good open-circuit values of 1.08 V. Moreover, maximum power point tracking experiments revealed a high stability and a further increase in efficiency could be observed over a long period of time, achieving finally a PCE of 4.25%.

Herein, three novel acceptor materials for organic photovoltaics based on perylene monoimides are represented and the PMI-hT-PMI/PBDB-T photovoltaic system is characterized, and first optimization attempts were performed.

Kurzfassung

Fossile Brennstoffe wirken sich stark negativ auf die Umwelt aus und sind für Treibhausgase verantwortlich, die zur globalen Erwärmung und Klimaveränderungen führen. Die Bedenken diesbezüglich nahmen drastisch zu, weshalb viele Forscher ihre Aufmerksamkeit auf alternative, umweltfreundliche Energiequellen gelenkt haben. Neben Wasserkraft, Windkraft und Biomasse ist die Photovoltaiktechnologie eine der vielversprechendsten, da die Sonne nahezu unbegrenzt Energie liefern kann. Aus diesem nachhaltigen Ansatz haben sich Solarzellen auf Silizium Basis entwickelt, woraus ihre kommerzielle Vermarktung erfolgte. Obschon Solarmodule sich am Markt etabliert haben, gibt es einige Aspekte, die durch weiterführende Forschung verbessert werden konnten, was zur Entwicklung der organischen Solarzellen führte, basierend auf Polymeren und kleinen Molekülen. Diese Verbesserungen sind geringeres Gewicht, Flexibilität, günstigere Herstellung und einfachere Produktion. Das Ziel dieser Arbeit war es, Akzeptormaterialien herzustellen, welche aus Perylenmonoimid (PMI) Komponenten bestehen, welche über Thiophen-, Hexylthiophen- oder Tetraphenylethen-Molekülen verknüpft sind. Die Synthese wurde über die Suzuki-Kreuzkupplung durchgeführt, die zu doppelt- und vierfach-verknüpften PMI Einheiten führte. Die Produkte wurden durch NMR-Spektroskopie und Massenspektrometrie charakterisiert und ihre optischen Eigenschaften wurden untersucht. Die Thiophenverbindung wies Löslichkeitsprobleme auf und das Reinigen des vierfach gekoppelten Tetraphenylethenprodukt stellte eine große Herausforderung dar. Die Hexylthiophenverbindung (PMI-hT-PMI) weist eine gute Löslichkeit, einen adäquaten Absorptionsbereich und passende Energieniveaus im Bezug auf das Donormaterial auf. Deshalb wurden Solarzellen auf Basis von PMI-hT-PMI hergestellt, gemischt mit einem konjugierten Polymer (PBDB-T) welches als Donormaterial fungierte. Diese organischen Solarzellen wurden hinsichtlich unterschiedlicher Donor/Akzeptor Verhältnisse und Temperaturen für das Tempern untersucht. Die Solarzellen erreichten vielversprechende Effizienzen von bis zu 3.35% mit guten Leerlaufspannungen von 1.08 Volt. Darüber hinaus zeigten Maximum Power Point Tracking (mpp) Experimente, dass die Solarzellen eine hohe Stabilität aufweisen und eine weitere Steigerung der Effizienz. Dies führte schließlich zu einer Effizienz von 4.25%. In dieser Arbeit werden drei verschiedene neue Akzeptormaterialien für die organische Photovoltaik Technologie vorgestellt. Weiters wurden Solarzellen mit einer Aktivschicht, bestehend aus PMI-hT-PMI/PBDB-T, charakterisiert und erste Optimierungsversuche hinsichtlich der Verbesserung der Effizienz durchgeführt.

Acknowledgments

At this point, I want to thank Prof. Gregor Trimmel for giving me the opportunity to live out my passion for chemistry and to work on such an interesting topic. The professional support and scientific advices of him and the members of his working group contributed to the success of this master thesis. Also, I want to acknowledge Petra Kaschnitz, Karin Bartl, Josefine Hobisch and David Pfeifer, who performed essential measurements for me.

Additionally my thanks go to the whole working group, including Stefan Weber and Bianca Prem, my friendly officemates who improved tremendously my computer skills and made my workaday office life cheerful, Matīss Reinfelds, for sharing his knowledge and his patience in explaining various scientific questions to me, Aileen Sauermoser, Birgit Ehmann and Marvin Paschek, for making the daily laboratory routine entertaining and amusing, Bettina Schweda, Peter Fürk, Indira Kopacic, Efthymia Vakalopoulou, Tomas Rath and Rene Nauschnig, for the nice talks during coffee breaks and gaming evenings. They have all created a pleasant working atmosphere.

Furthermore, I would like to thank my parents and lovely sisters, who gave me so much strength throughout my whole studies. Also, I want to mention my precious friends, especially Isabella Pfusterer, who always supported and motivated me, even 500 miles away.

At last I want to thank Fabian Außersteiner, who is continuously inspiring me and brightening up every day of my life.

Table of Contents

1. Introduction

The Sun represents the center of our solar system and was formed 4.5 billion years ago, during the collapse of dust and gas, called nebula. Amongst other layers, it consists of a core where about 600 million tons hydrogen fuse into helium every second. This process generates energy which is carried by light particles called photons. When the solar photons emerge by the fusion of two protons in a nucleus of deuterium, it takes them approximately eight minutes to cover the distance of 150 million kilometers in order to reach the surface of earth. This distance is referred to as ‘astronomical unit’ (AU). By holding the whole solar system together, the Sun represents an indispensable center for life on Earth, creating space weather and providing Earth with energy, heat and light.[1]

Thus, sunlight has a major influence on life on Earth, such as plants, animals and humans. The human eye consists of photoreceptor rods and cones that enable the perception of the visible range of the sunlight spectrum from ~ 380 nm (violet) up to ~ 740 nm (red). In addition, the human skin uses the near-ultraviolet range of the spectrum for the synthesis of the very important vitamin D. As far as plants are concerned, photosynthesis is a unique feature of nature that uses visible sunlight to convert H_2O and CO_2 into oxygen and sugars.

The first discovery in the field of photovoltaics was made with the help of an electrolytic cell by the French physicist Alexandre Edmond Becquerel over 181 years ago, in 1839. By illuminating platinum or gold electrodes, coated either with AgCl or AgBr, placed in an acidic solution, he found out that some material is able to create voltage and current upon irradiation.[2] This effect is called the photovoltaic effect. The scheme of the apparatus designed by Becquerel is depicted in Figure 1.

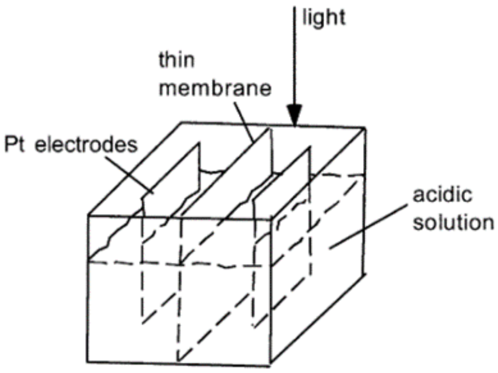

Figure 1. Design of the apparatus by A. E. Becquerel.

In 1873 Willoughby Smith discovered the photosensitive property of selenium.[3] Further findings and developments in directions of solar cells were made by William G. Adams and Richard E. Day, who were also the first to perceive the photovoltaic effect created by illuminating junctions between platinum and selenium. These findings paved the way to producing the first selenium solar cell assembly which was constructed in 1877.[4] Soon after in 1883, the American inventor Charles Fritts fabricated the first selenium solar panels and described the production process in detail.[5]

In 1905 Albert Einstein, described the nature of light and the photoelectric effect, which is also fundamental in photovoltaic technologies. For his theoretical work, he was awarded the Nobel Prize in physics for “his discovery of the law of the photoelectric effect” in 1921.[6] The photoelectric effect is a phenomenon that describes the release of electrically charged particles from some materials when exposed to electromagnetic radiation. One unexpected observation showed that the maximum kinetic energy of these released particles does not vary with light intensity, which in turn contradicts the wave theory. Hence, Albert Einstein formulated a new theory of light which defines light particles as having a certain amount of energy. The amount of energy, which a light particle contains, depends on the frequency of light.[7,8] In 1914 Robert A. Millikan put Einstein’s hypothesis of the photoelectric effect into practice by performing an experiment called the oil drop experiment. For “his work on elementary charge of electricity and on the photoelectric effect”, Milikan was also awarded the Nobel Prize in 1923.[9]

The next development in photovoltaic history was made by the American engineer Russell S. Ohl from Bell Laboratories in 1939, who focused on the research towards the behavior of certain crystals. During the investigation of silicon samples, he found out that the sample having a crack in the middle could generate current when exposed to light. The sample was then fractioned into a positively doped side and a negatively doped side, due to different impurity levels accidentally originating from the crack. This led to the generation of an electric field and Ohl’s accidental invention of the p-n junction, which is fundamental for solar cells.[10,11]

In 1941, Russell S. Ohl additionally investigated the effect of doping semiconducting materials with foreign atoms. Thus, new properties can be attributed to these materials, becoming suitable for solar cells. In that year, the very first solar cell was manufactured.[11]

The first modern solar cells, consisting of single crystal silicon wafers with p-n junction, were built by Chapin, Fuller and Pearson at Bell Laboratories in 1954 and reached efficiencies of about 5 %.[12] The now commercially available photovoltaics with either single or polycrystalline silicon wafers still resemble those from Bell Laboratories. However, the efficiency has improved over the years. An overview of the evolution of different solar cell technologies and their corresponding efficiencies is depicted in Figure 2.[13]

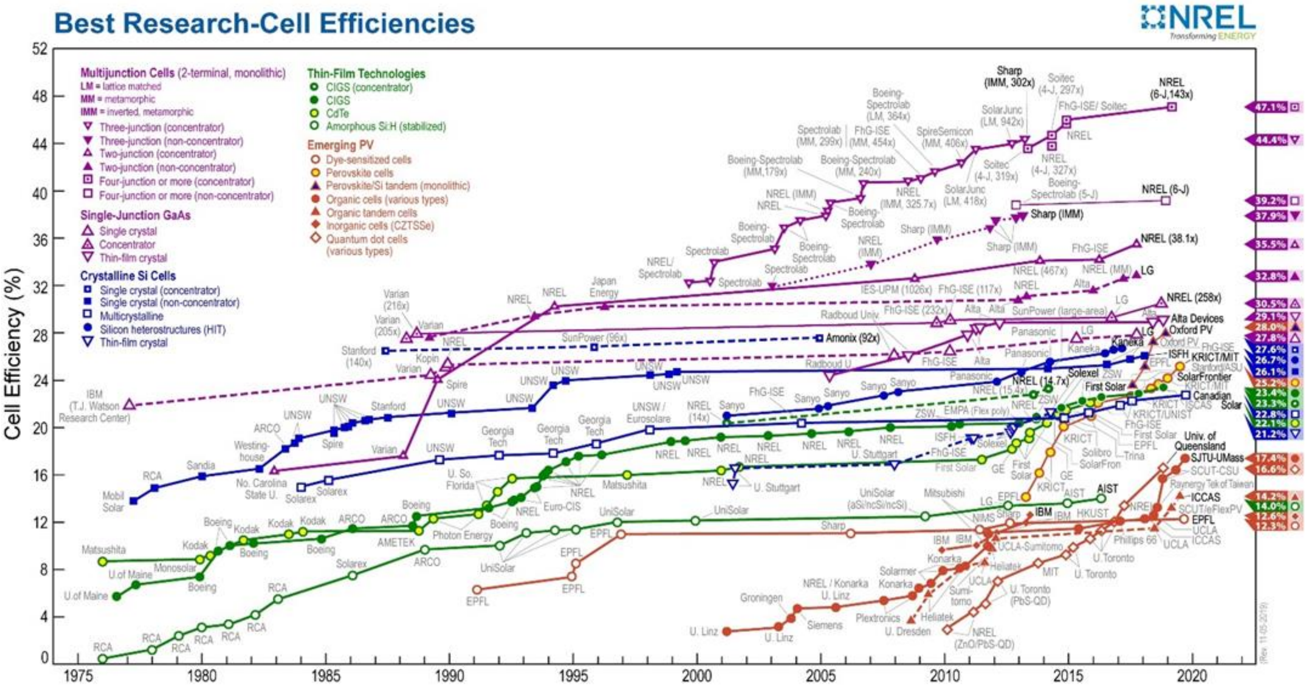

Figure 2. Graphical demonstration of the evolution of different solar cell technologies with respective efficiencies (© NREL).[13]

Figure 2 shows that conventional single-crystal silicon solar cells exhibit a power conversion efficiency of 26.1%. By using lenses and mirrors to focus the sunlight, concentrated photovoltaics, comprising of multiple p-n junction, reaches PCE values as high 46%.[14] This technology enables the absorption of a wider range of wavelengths.[15] Moreover, poly-crystalline silicon solar cells demonstrate a PCE of 22.8%, whereas amorphous silicon, cadmium telluride and CIGS ($CuIn_{(1-x)}Ga_{(X)}Se_2$ materials) form the group of thin-film technologies have an efficiency range from 14.0% and 23.4%. Since 2001 the solar cell technologies have been further developed and the emerging technologies comprise of perovskite cells, dye sensitized solar cells (DSSC), quantum dot cells, inorganic (CZTSSe) and organic solar cells.

2. Theoretical Background

2.1. Organic solar cells in general

The research towards organic solar cells (OSC) is ongoing, due to many advantages over traditional silicon-based photovoltaics. The advantages range from improved solution-processability, the potential of exhibiting transparency and the capability of roll-to-roll printing technologies up to high mechanical flexibility, leading to better incorporation of photovoltaic elements in architecture. [16,17,18] Since OSCs have come into focus of research, the efficiency development had a tremendous increase observed over the last two decades (see Figure 2). Additionally, the findings resulting from the investigation of light-emitting diodes led to major improvements in the development of organic photovoltaics, since LEDs possesses similar technologies.

The ability of semiconducting organic materials to absorb light in the (UV)-visible range of the solar spectrum and the transport of current results from the sp^2 hybridization of the integrated carbon atoms. The carbon atoms in a conducting polymer that exhibits electrons in the p_z-orbital of each sp^2 hybridized carbon, leading to the formation of π-bonds in between neighboring carbon atoms. This leads to the dimerization effect, e. g. a structure with alternating double and single bonds. Due to this fact, semiconducting polymers reveal high electronic polarizability.[19]

The much lower charge-carrier mobility of semiconducting materials used in OSC, which affects the cell design and power conversion efficiencies, is a disadvantage in comparison to inorganic silicon-based solar cells.[20] Nevertheless, the large absorption coefficients of semiconducting organic materials with more than 10^5 M^{-1} cm^{-1} outweighs the low mobilities. Therefore, very thin devices of typically less than 100 nm are efficient enough to achieve high absorption. In contrast to crystalline inorganic semiconductors, organic materials show amorphousness and disorders and exhibit smaller diffusion lengths of excitons, which are, amongst others, responsible for the low efficiencies. The higher exciton binding energies in OSC lead to higher required electric fields in order to dissociate them into free charge carriers. Besides, degradation issues of solar cells need improvement. [19,21,22] However, the possibility of chemically modifying organic materials, varying electronic properties like band gaps, and low costs of large-scale production lead the investigations towards OSC forward. Although the PCEs of organic solar cells are remarkably lower than other photovoltaic technologies show, Meng et al. achieved to build organic solar cells in a tandem cell strategy with the highest efficiency by date of 17.3%.[23]

2.2. Working principle of organic solar cells

In general, the active layer of OSCs consist of an electron acceptor and electron donor material, both absorbing light. By the absorption of a photon exhibiting a sufficient amount of energy, excitons are formed subsequently in the donor and acceptor material.

The basic principle of converting light into electricity in organic solar cells is divided into four steps (see Figure 3): (a) formation of excitons, an excited state consisting of electron-hole pairs contracted to each other by electrostatic interactions, (b) diffusion of excitons at the donor/acceptor interface where the next step (c) charge separation takes place, leading to the last step (d) the charge transport. In the last step, holes are transported to the cathode and electrons to the anode, providing electric current to the consumer load.[24]

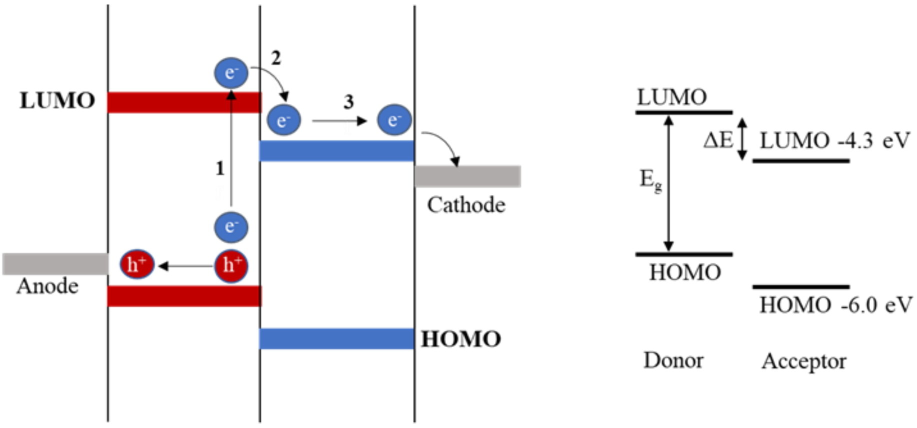

Figure 3. Exciton dissociation at donor/acceptor interphase.[22]

At the donor/acceptor interface, the charge separation of electron-hole pairs occurs.[25] Conjugated polymers often act as donor materials due to their delocalized π-electrons, which can be excited by light in the range of the visible part of the solar spectrum. Thus, during the absorption of light, the electron (e^-) in the donor material is transferred into the lowest unoccupied molecular orbital (LUMO), whereas a hole (h^+) is left in the highest occupied molecular orbital (HOMO). This phenomenon is then referred to as 'exciton'. To cause dissociation, the acceptor must counterbalance the binding energy of the exciton in the donor, hence the charge transfer at the interface can only occur when:

$$E_A^A - E_A^D > U_D \tag{1}$$

where E_A represents the electron affinity of acceptor and donor (subscript A and D), respectively, and U_D is defined as the binding energy of the exciton. Figure 3 shows the dissociation process graphically. If the E_A of the acceptor is greater than of the donor, the generated electron will hop into the LUMO of the acceptor. If the HOMO of the acceptor is lower than in the donor, the hole will successfully dissociate.[22]

The current of a solar cell is attributed to the amount of created charges that the electrodes collect. This amount is based on the part of photons that are absorbed (η_{abs}), the part of electron-hole pairs that dissociates (η_{diss}) and the fraction of charges reaching the electrodes (η_{out}). The overall photocurrent (η_j) is defined as:

$$\eta_j = \eta_{abs} \cdot \eta_{diss} \cdot \eta_{out} \tag{2}$$

The portion of photons being absorbed is a function of the absorbing layer thickness, absorption coefficient, absorption spectrum and internal reflections, due to metallic electrodes. The dissociating electron-hole pair fraction depends on whether they dissociate into a charge separation region and on the probability of charge separation in that region.[26] Furthermore, the driving force for the charge carriers to reach the electrodes is attributed to the gradient of electrochemical potential of electrons and holes. This results from two forces: the concentration gradient of the charge carrier species, leading to a diffusion current, and the internal electric fields, resulting in a field induced drift.

The energy difference between the HOMO and LUMO level of a material is determined as the bandgap.

Considering the probability of dissociation, it is more likely for excitons to dissociate if the potential difference between LUMO of the donor and LUMO of the acceptor is augmented. The potential can be increased by selecting different semiconducting materials with a large offset (ΔE, see Figure 3), resulting in an increased V_{bi} and larger V_{OC}. The V_{bi} is determined as[27]:

$$V_{bi} = E_{LUMO\,(Acceptor)} - E_{HOMO\,(Donor)} \tag{3}$$

The open-ciruit voltage (V_{OC}) and the built-in potential (V_{bi}) are defined as the difference between the HOMO of the donor and the LUMO of the acceptor.[27] Based on empirical analysis, Scharber et al. determined the definition of V_{OC} in relation to the built-in potential by the following equation[27]:

$$V_{OC} = V_{bi} - 0.3 \tag{4}$$

The solar cell characteristics V_{OC}, I_{SC}, FF and PCE will be discussed in Chapter 2.4.

2.3. Solar cell device architectures

2.3.1. Bilayer heterojunction

The so-called bilayer heterojunction device comprises the acceptor and donor layer, which are stacked together, resulting in single common interface inbetween. The layers are brougth together by sequencial thermal deposition of the adjacent materials (donor and acceptor). Due to the drastic potential drop between the two layers, the charge separation takes place at the interface. Hence, the bilayer is sandwiched between two conductive metal electrodes matching the HOMO of the donor and the LUMO of the acceptor to maintain the extraction of charge carriers.[19] A scheme of the bilayer solar cell device is depicted in Figure 4.

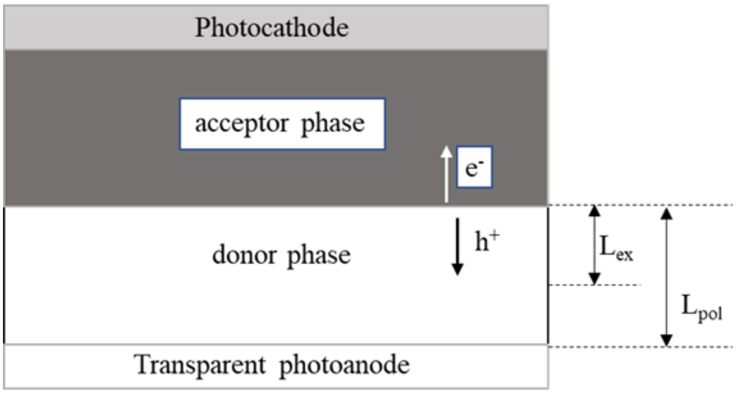

Figure 4. Scheme of the bilayer heterojunction solar cell device. Lex defines the exciton diffusion length and Lpol represents the domain size of the donor phase.

The most commonly used anode material is indium tin oxide (ITO), which is the best choice due to its transparency for capturing the incident light.[28] Power conversion efficiencies of 3.5% can be reached with solar cells based donor and acceptor materials spin-casted, forming a well-defined planar interface bilayer heterojunction.[29] The disadvantage of bilayer heterojunctions can be explained by the exciton diffusion length. The exciton diffusion length L_{ex} can be defined as the average length an exciton can diffuse within a polymer material, before the electron and hole recombine, resulting in an annihilation of the charge carrier. If the exciton diffusion length is much smaller than the average pathway an exciton must travel through the material to reach the heterojunction, recombination of charge carriers is favored. This is the case in bilayer heterojunction systems, beacause nearly all excitons are generated in a larger distance to the heterojunction interface than L_{ex} (see Figure 4). Therefore, relatively small PCE values can be reached in bilayer heterojunction solar cell devices.[30] However, this problem can be circumvented by introducing the bulk heterojunction concept.

2.3.2. Bulk heterojunction

The basic principle of bulk heterojunction (BHJ) is to mix the donor and acceptor material in a bulk volume, creating donor/acceptor interfaces smaller than the exciton diffusion length. Hence the interface of the semiconducting materials in BHJ solar cells is randomly dispersed throughout the bulk volume. Due to the increased interface surface, the recombination losses can be reduced drastically. However, the fraction of spatially interrupted pathways for charge carriers pose a disadvantage compared to bilayer heterojunction.[19] The schematic depiction in Figure 5 shows the bulk heterojunction in solar cell device.[30]

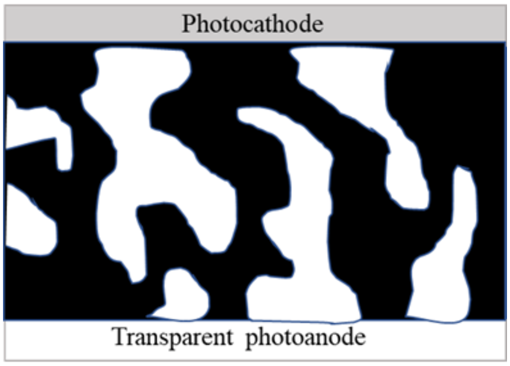

Figure 5. Bulk heterojunction solar cell device, black demonstrating the acceptor and white the donor material.

2.4. Characteristics of solar cells

In general, an I-V curve is the graphical demonstration of the relationship between the open-circuit voltage (V_{oc}) and the short-circuit current (I_{sc}). By measuring the I-V curve, characteristic parameters of a solar cell device can be obtained, including V_{oc}, I_{sc}, the fill factor (FF) and the power conversion efficiency (PCE). The schematic illustration is depicted in Figure 6.

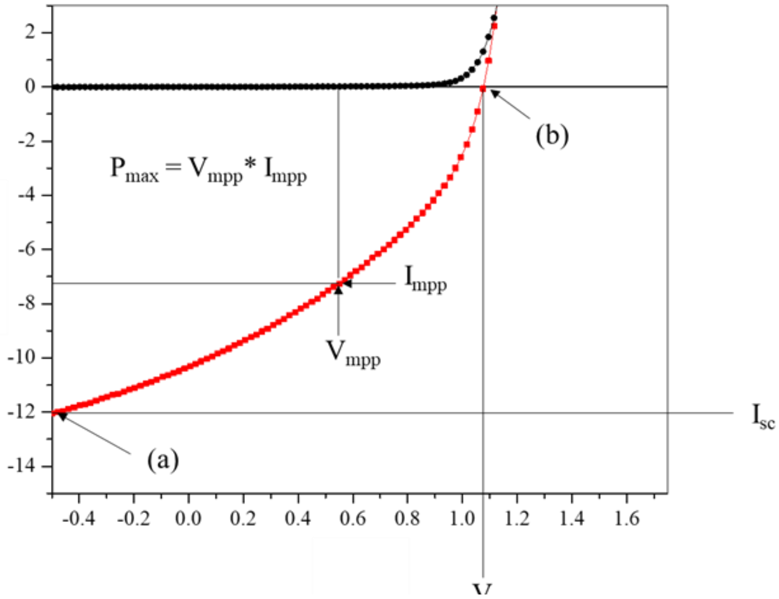

Figure 6. Typical I-V curve for the characterization of solar cells.

The I_{sc} determines the maximum photocurrent under short-circuit conditions when the voltage is zero as depicted Figure 6/(a). On the other hand, V_{oc} indicates the 'flat band conditions', where no current flows, as shown in Figure 6/(b). The generated power in a solar cell is revealed in the fourth quadrant of the I-V curve (voltage multiplied by current).[19] The maximum power point (MPP), as the name implies, is the point in which the solar cells delivers the maximum power. It can be located where the product of voltage and current is the largest. These parameters are incorporated in the calculation of the fill factor (FF):

$$FF\ [\%] = \frac{I_{mpp} \cdot V_{mpp}}{I_{SC} \cdot V_{OC}} \tag{5}$$

The power conversion efficiency is the ratio between the maximum output of power and the input of solar irradiance, and can be written as in equation (6):

$$PCE\ [\%] = \frac{P_{out}}{P_{in}} = \frac{I_{mpp} \cdot V_{mpp}}{P_{in}} = \frac{FF \cdot I_{SC} \cdot V_{OC}}{P_{in}} \tag{6}$$

The parameters P_{out} and P_{in} respectively, are given in W/cm^2 and, for better comparison possibility, the I_{SC} is given as the short-circuit current density in A/cm^2, taking the actual electrode area into account.

2.5. Materials used in organic solar cells

2.5.1. Donor Materials

Conjugated polymers are capable of becoming electron donors upon photoexcitation and are often assembled in organic solar cell devices. Modern donor materials can improve the I-V characteristics, comparing to earlier polymers, resulting in better efficiencies. The most common donors with their respective abbreviated nomenclature are depicted in Figure 7.[31,32,33]

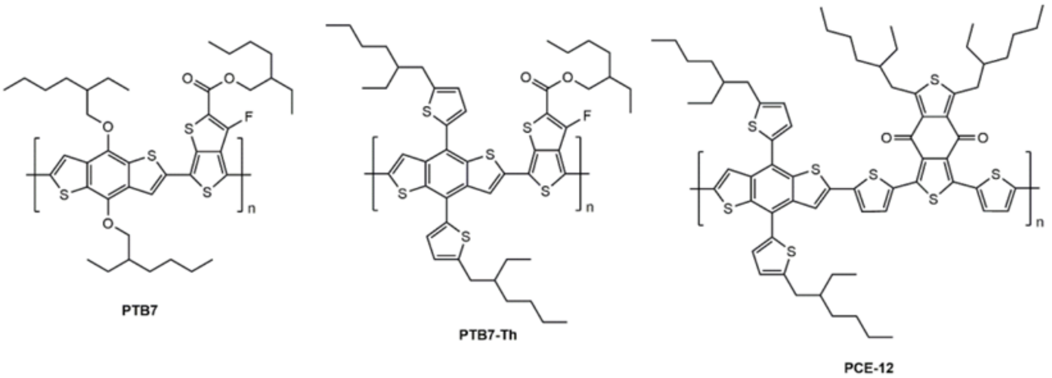

Figure 7. Most common donors used in OSC.

The requirements to function as a good polymer donor are high absorption coefficients, high carrier mobilities, good solubility, medium or low band gap and matched energy levels (in respect to acceptor).[34]

2.5.2. Acceptor Materials

One of the most used acceptor materials are $PC_{60}BM$ and $PC_{70}BM$, which are based on a fullerene C_{60} buckyball structure (see Figure 8).[35]

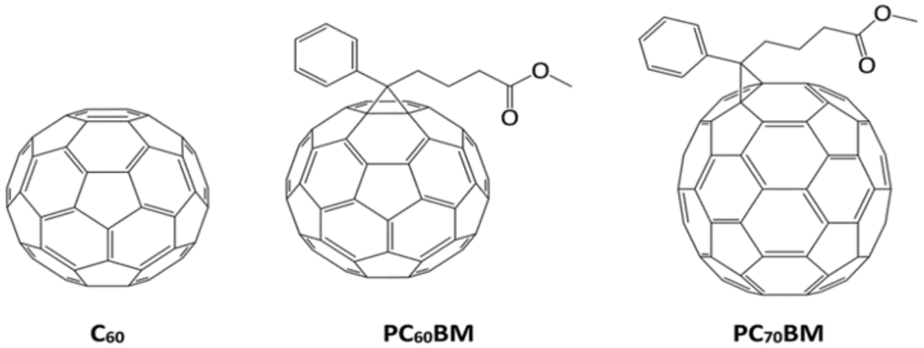

Figure 8. Common fullerene-based acceptor materials for organic solar cells.[35]

They exhibit suitable properties like good charge transfer, excellent possibility of splitting excitons when blended with a donor material and high electron mobilities. However, the poor tunability of the structure and low absorption in visible region of the solar spectrum pose some drawbacks.[36] The use of fullerenes in OSC is also rather limited due to high production costs and photochemical and thermal instabilities.[37] Therefore, the attention was recently shifted towards non-fullerene-based acceptors, which show easier synthesis procedures and offer larger possibility to tailor their properties. The research towards perylene-based acceptors (see Figure 9) is ongoing and the development has extended over the past years in order to find alternatives to the fullerenes.

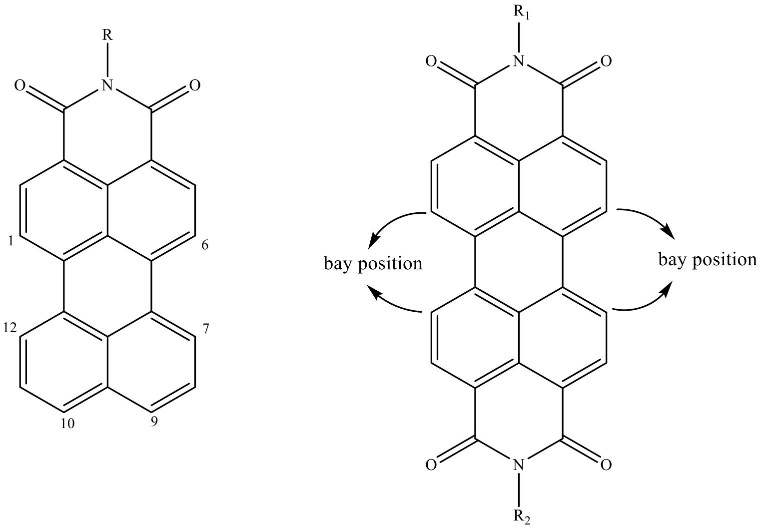

PMI

PDI

Figure 9. Perylene monoimide and diimide acceptor molecules, used in OSC applications.

Considering this new type of acceptors, the perylene-diimide and perylene-monoimide are often in the focus of research. By the possibility of functionalizing the perylene structure either in imide-position or bay-position, a variety of different features can be achieved concerning the electronic, physical, optical and aggregation properties.[38] In addition, the coupling of the perylene molecules with some linkers in between is frequently the objective in recent investigations.[39]

Besides the active layers in an organic solar cell, it is possible to further improve the efficiency by introducing an interfacial layer between the active layer and the electrodes. That is likewise known for LED type devices, in which the insertion of a thin layer of LiF or CsF improves the charge injection and lowering the interface barrier. Also, for organic solar cells, the application of a LiF layer can improve the contact efficiency.[40] Further functions of the interfacial layers used in OSCs like ZnO_x or TiO_x comprise the protection of the active layer from diffusion, protection of current leakage and the function as an optical spacer.[41]

2.6. State of the Art

In the beginning of the 1910s, Kardos firstly perceived to synthesize and apply the highly conjugated perylene-3,5,9,10-tetracarboxylic diimides (PDIs) as textile dyes and high-performance pigments in violet, red and even black shades.[42] Decades later, PDIs and their derivatives have been used to the purpose of fingermark detection, living cell staining, LEDs and organic photovoltaics.[43,44,45] There exist several synthetic routes in order to modify the optical and electronic properties of PDIs by functionalization of the bay positions (see Figure 9). Another important building block for the synthesis of acceptor materials in photovoltaics are the asymmetric perylene monoimides (PMIs). When functionalizing the position 9 in PMI, it is possible to initiate major changes concerning the electronical and optical properties.

Besides organic solar cells, research also goes towards dye-sensitized solar cells (DSSC). The first report of a successfully produced photovoltaic device based on a Ruthenium complex as sensitizer was published by Grätzel in 1991.[46] Due to its high power conversion efficiencies of 7%, DSSC technology got in the focus of further developments. Since perylene imides, mainly perylene monoimides (PMI), can be easily functionalized with anhydride groups or carboxylic acids in order to exhibit an anchor for the attachment onto inorganic semiconductors, they have also been used as sensitizers in DSSC.

The first breakthrough involving perylene diimides was reported by L. Schmidt-Mende et al. in 2001.[47] Herein, a soluble unsubstituted PDI derivative and a hexa(alkylphenyl)-substituted hexabenzocoronene were processed to fabricate photovoltaic devices with efficiencies of ~ 2%, forming segregated structure with high interfacial layers. Additionally, in 2006 Dierschke et al. found out that using PDI blended with poly-carbazole as donor led to better efficiencies than applying the well-established fullerene-based $PC_{61}BM$ acceptor.[48] However, PCBM and their derivatives constitute generally more promising acceptor materials in photovoltaic despite the superior performance in this singular example.

Polymer solar cells based on poly(3-hexythiophene) (P3HT) blended with PCBM exhibit PCEs of up to 5%, while the corresponding counterpart devices with PDI:PCBM as active material only reach 0.19%.[49]

In 2007, Zhan et al. used PDI compounds in all-polymer solar cells (all-PSC) in a ITO/PEDOT:PSS/active layer/Al structure. They synthesized a perylene diimide polymer with dithienothiophene attached in the bay position and used it as an acceptor, mixed in a blend with a polythiophene polymer derivative. Average power conversion efficiencies of about 1% were reached.[50]

Furthermore, strong aggregations are an issue, formed due to molecular packing of the PDI moieties, resulting in intermolecular charge recombination and lower efficiencies.[49] By introducing functionalized groups in the bay-positions of PDIs, it is possible to suppress the aggregation between PDI compounds. To that end, diphenoxylated PDIs were investigated in 2010 as acceptor molecules in BHJ solar cells. In this case, PDI was mixed with small molecules or polymers in a blend for bulk heterojunction, reaching a power conversion efficiency of 2.85% with a J_{SC} of 6.8 mA cm^{-2}, a V_{OC} of 0.88 V and a fill factor of 0.47.[51] The PCE was increased to 3.17% by adding ZnO as an interfacial layer.

In 2011, another all-PSC system was investigated, including PDIs, which were copolymerized with different electron-rich units (donor-segments). These solar cells, consisting of PDI-copolymers as acceptors and polythiophene derivatives as the donor material, achieved PCE values of 2.23%.[52]

Moreover, the formation of tetrahedral configurations of PDI moieties (3D-like structure) is possible and was published by Wangqiao Chen et al. in 2015.[53] The acceptor molecule exhibits appropriate energy levels referred to the donor material and a complementary absorption. The devices reached power conversion efficiencies of up to 2.73%.[53]

Later in 2015, alkoxy-substituted PDI dimer compounds were prepared, reaching a PCE of 6.3%.[54] The combination of a difluorobenzothiadiazole based donor, namely PffBT4T-2DT, and a PDI dimer acceptor (linked in bay position) led to the high V_{oc} of 0.98 V.

Yan et al. investigated a small-molecule acceptor in 2016, consisting of two PDI moieties linked by a spirofluorene unit, reaching impressive power conversion efficiencies of 9.5%, high V_{oc} of 1.11 V and internal quantum efficiencies of nearly 90%. [55]

Contrary to PDIs, PMIs show less symmetry in the structure but show similar π-π overlapping of the aromatic cores (π-π interactions).[49] PMIs show higher LUMO energy levels than fullerene derivatives, lowering the probability of the electron transfer from donor to acceptor, but at the same time increasing the V_{OC}. Besides, PMIs show lower absorption coefficients than PDIs, but also higher-lying LUMO levels, which can be beneficial for the open-circuit voltages. Nevertheless, perylene monoimides were recently investigated towards acceptor materials in BHJ organic solar cells.

In 2005 and 2006, Cremer et al. published perylene-oligothiophen dyad, triad and star-shaped systems for the application in photovoltaics (see Figure 10).

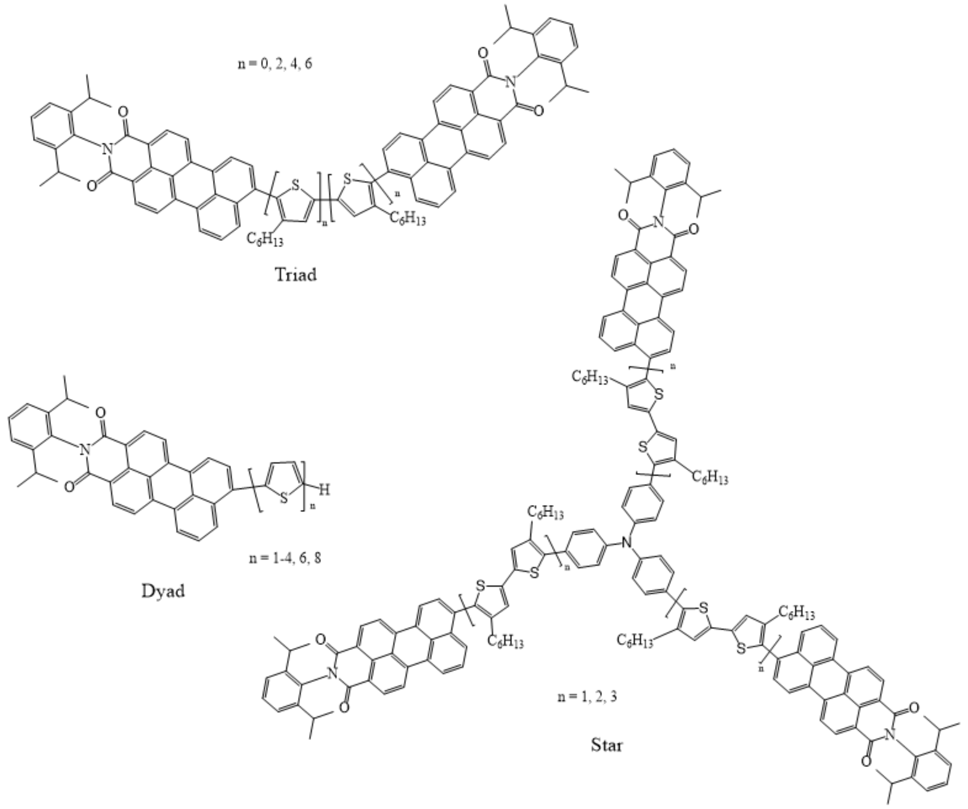

Figure 10. Dyad, triad and star-shaped hybrid acceptor system for photovoltaic application investigated by Cremer et al.[56,57,58]

Herein, the acceptor molecules are based on PMI and their photovoltaic and electronic properties of these novel systems were investigated.[56,57,58] The perylene moieties provide high absorption in the visible range, while thiophen-based systems have excellent charge transport properties and improve the absorption in shorter wavelengths. The best results reached the perylene monoimide-octathiophen dyad (compound 73 with n=8, see Figure 10) with a PCE of 0.84% and a V_{OC} of 0.94 V. The triad system exhibits a PCE of 0.2% and the star-shaped compound a PCE of 0.25%.

In 2015, Zhang et al. developed fluorene-linked perylene monoimide acceptors (PMI-F-PMI) with PCEs of 2.3%, showing a non coplanar configuration with distorted angles between fluorene and PMI. The high V_{oc} value of 0.98 V results from the effect, that the LUMO of the acceptor matches well with the donor material P3HT.[59] Further research of Zhang et al. led to another solar cell device containing the PMI-F-PMI acceptor material coupled with a bithienyl-benzodithiphene-based donor material, showing high excition dissociation efficiencies. By a solvent additive treatment, V_{oc} values as high as 1.3 V were reached with a power conversion efficiency of 6%.

In 2017, Hu et al. investigated perylene monoimide moieties linked by different aryl molecules as shown in Figure 11.[39] Due to π-π stacking, PMIs are moderately soluble, making purification processes and further applications challenging.[60]

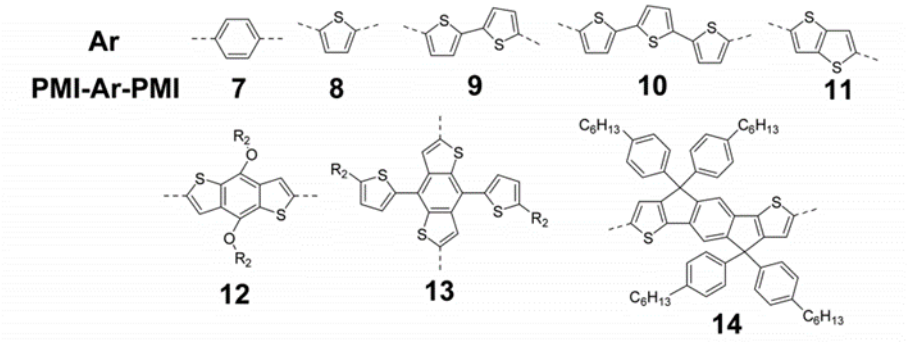

Figure 11. PMI-Ar-PMI acceptor materials with different linkers (7-14) investigated by Hu et al.[39] Adapted with permission from (Hu, Y.; Chen, S.; Zhang, L.; Zhang, Y.; Yuan, Z.; Zhao, X.; Chen, Y. *J. Org. Chem.* 2017, 82 (11), 5926-5931). Copyright 2020 American Chemical Society.

The highest PCE value was obtained with the linker 9 based on two thiophene units (see Figure 11), achieving 1.3%.[39]

In 2019, a PMI compound linked with alkyne units (n=0, 1, 2) was investiged towards ternary OSC (donor/acceptor 1/acceptor 2) and used as an additional acceptor molecule besides ITIC. The linked PMI based molecule was employed as a second acceptor, in order to adjust the energy levels, modify morphologies and thus enhancing FF, V_{oc} and J_{sc} values. Herein, PCE values of 9.77% were reached.[61]

So far, concerning organic solar cells in general, the best efficiencies were obtained in 2019 by the working group of Yong Cui et al. using a chlorinated acceptor molecule combined with the donor PBDB-TF. The obtained power conversion efficiencies of 16.5%, and the J_{SC} reaches high values of 25.4 mA cm^{-2}, resulting from the chlorination which is broadening the optical absorption.[62]

2.7. Suzuki Miyaura Coupling

The Japanese scientists Tamao and Kumada already found in 1972 that Ni(II) complexes can catalyze the reaction of organomagnesium compounds with aryl and alkenyl halides.[63] Moreover, regarding cross-coupling, Kochi et al. found in 1975 that Fe(III) complexes are adequate catalysts for the reaction of Grignard reagents with Li_2-$CuCl_4$ and 1-halo-1-alkenes in order to get haloalkanes.[64] In 1975, Murahashi et al. where the first to discover that $Pd(PPh_3)_4$ also catalyzes Grignard reactions.[65] Besides, many other organometallic compounds can be used as nucleophiles for cross-coupling reactions, such as organostannanes (Stille coupling[66]), organolithiums, copper, magnesium, mercury, zirconium, 1-alkenylcopper and organosilicon compounds. The Suzuki-Miyaura reaction also belongs to the class of cross-coupling reactions and the results of research were first published in 1979 by the Japanese chemist and Nobel Prize laureate Akira Suzuki.[67] The Nobel Prize in Chemistry was awarded to Suzuki A., Richard F. Heck and Ei-ichi Negishi for 'the discovery and development of palladium-catalyzed cross coupling reactions in organic synthesis' in 2010.[68] The general reaction scheme is depicted in Figure 12.

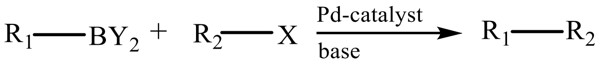

$$R_1—BY_2 + R_2—X \xrightarrow[\text{base}]{\text{Pd-catalyst}} R_1—R_2$$

Figure 12. Scheme of the Suzuki cross-coupling reaction.

The organoboron compound $R_2 – BY_2$ is coupled with a halide $R_2 – X$, in presence of a palladium catalyst and base, to generate a new carbon-carbon bond in the product $R_1 – R_2$. The mechanistic steps of the cross-coupling are shown in Figure 13.

The general catalytic cycle involves oxidative addition – transmetallation – reductive elimination parts. This typical cycle is observed in cross-coupling reactions containing catalysts like Pd(0), Ni(0) and Fe(I). Although each step contains particular complex processes, the intermediate compounds Ar-Pd(II)X$(L)_2$ and Ar-Pd(II)$(L)_2$-Ar^I were successfully isolated and characterized by spectroscopic methods.[69] Firstly, oxidative addition of an aryl-halide to the palladium(0) catalyst takes place to form the Pd(II)-complex Ar-Pd(II)X$(L)_2$.

By the transmetallation of the organoboron species Ar^I-$B(OH)_2$ with Pd(II), the diaryl-palladium complex is formed and furthermore isomerization from trans to cis leads to the formation of Ar-Ar^I, by a reductive elimination step. In the last step, the catalyst is regenerated and can react further again. In addition, the frequently occurring side-reaction, the so-called homocoupling[70], is marked in Figure 13.

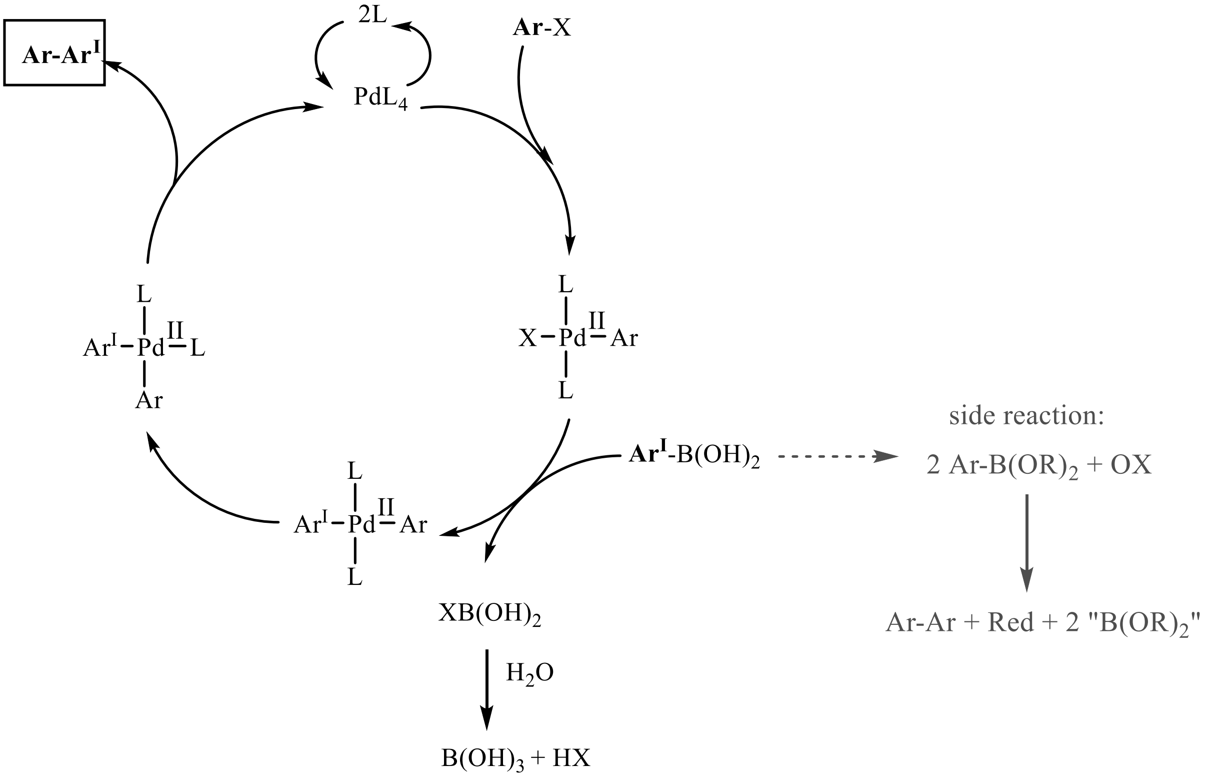

Figure 13. General scheme of mechanistic steps in the catalytic cycle of Pd-catalyzed. Suzuki-Miyaura cross-coupling reaction.[69]

The leaving group 'X' influences the reactivity of the Suzuki-coupling reaction and is ordered in the following sequence: I > Br > OTf > Cl > F.[71]

3. Objective

Since non-fullerene-based acceptor materials are promising for the purpose of the organic solar cells (OSCs) and furthermore have the potential to outperform the well-established fullerenes, the objective of this work was the synthesis of perylene monoimide (PMI) based acceptor materials. Therefore, PMI moieties were coupled via Suzuki-coupling with three different linker units, in order to obtain the desired acceptor materials as depicted in Figure 14. The compounds are characterized using ^{1}H-NMR spectroscopy to confirm the respective structures. To determine whether the products are suitable to function as acceptors in OSCs, HOMO/LUMO levels were calculated using density functional theory and absorption and emission spectra were recorded using UV-Vis spectrometry.

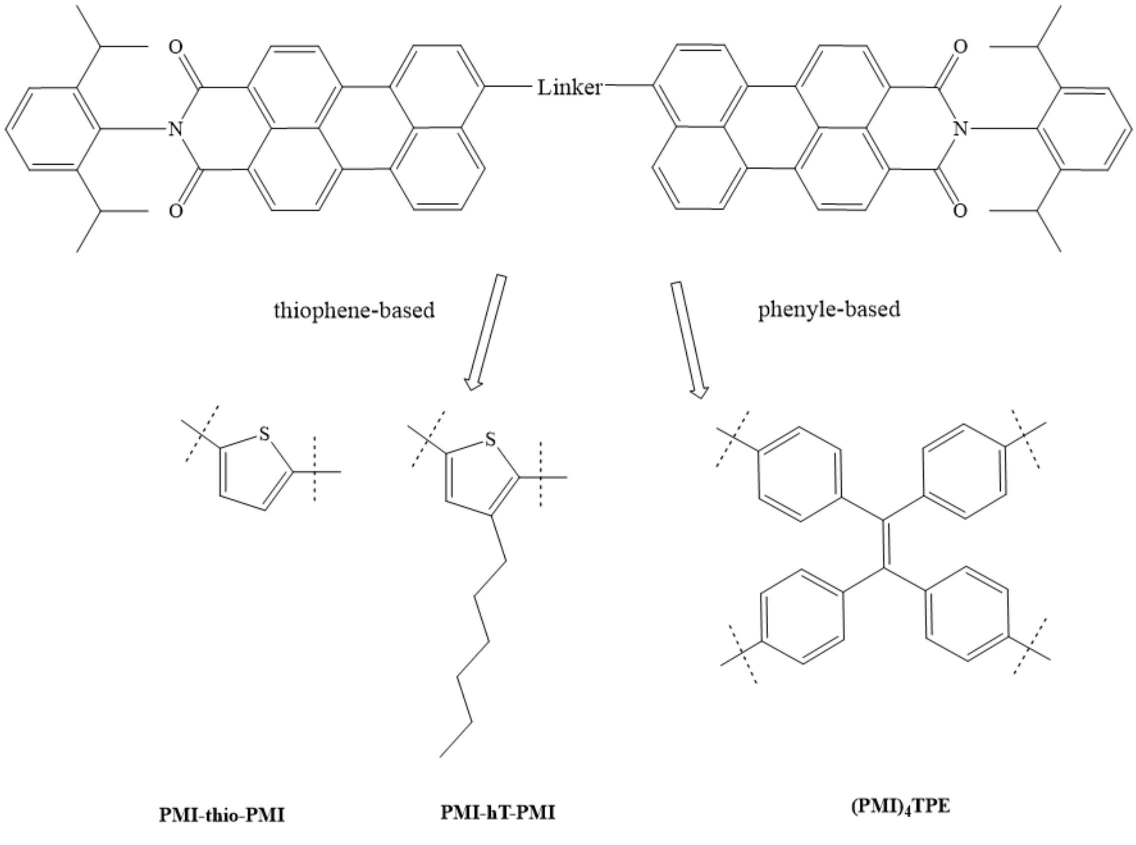

Figure 14. PMI based acceptor materials synthesized for the purpose of organic photovoltaic application.

4. Results and Discussion

4.1. Density Functional Theory Calculations

In order to examine the geometrical conformations and optical properties of the thiophene-linked perylene monoimides, DFT calculations were done together with Matīss Reinfelds. In the first instance, the geometric optimization of the two molecules was done using the B3LYP functional and 6-31G* (d, p) as basis set (Gaussian 09)[72]. In addition, another basis set 6-31+G (d, p) was performed, which takes the diffusion of electrons in the molecule into account. The results, including HOMO/LUMO levels and UV-Vis excitation with the respective oscillator frequencies (f) and excitation energies are summarized in Table 1 for PMI-thio-PMI and PMI-hT-PMI.

Table 1. HOMO/LUMO levels and UV-Vis excitation results for PMI-thio-PMI and PMI-hT-PMI.

				UV-Vis excitation (S_0-S_1)		
Molecule	**Basis set**	**HOMO [eV]**	**LUMO [eV]**	**Excitation energy[eV]**	**f**	**Absorption max. [nm]**
PMI-thio-PMI	6-31G(d,p)	-5.48	-3.05	2.17	1.38	572
PMI-thio-PMI	6-31G+(d,p)	-5.75	-3.37	2.11	1.38	588
PMI-hT-PMI	6-31G(d,p)	-5.51	-2.98	2.26	0.24[a]	548
PMI-hT-PMI	6-31G+(d,p)	-5.78	-3.31	2.20	0.26[b]	563

a: S_0-S_2 transition is predicted to have a larger oscillator strength (1.28) and is located at 2.38 eV (520nm). b: S_0-S_2 transition is predicted to have a larger oscillator strength (1.24) and is located at 2.31 eV (536 nm).

Moreover, the dihedral angles were determined for both compounds. The graphical description is depicted in Figure 15.

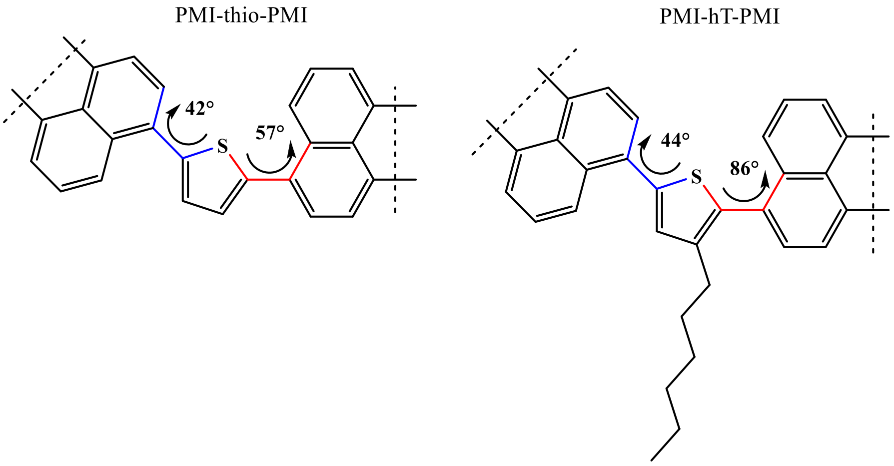

Figure 15. Dihedral angles determined by DFT calculations for the thiophene-linked compounds.

Regarding the angles indicated in red (see Figure 15), the hexyl thiophene exhibits a value of 86°, in comparison to the thiophene compound with a much smaller angle of 57°. Since the PMI-hT-PMI contains a hexyl chain, the molecule has to orient differently in order to get an energy minimum, thus the angle is greater, and the molecule shows less planarity.

The calculated HOMO/LUMO levels of PMI-thio-PMI and PMI-hT-PMI are shown graphically in Figure 16. The pictures a) and b) were obtained by natural bond orbital (NBO) analysis.

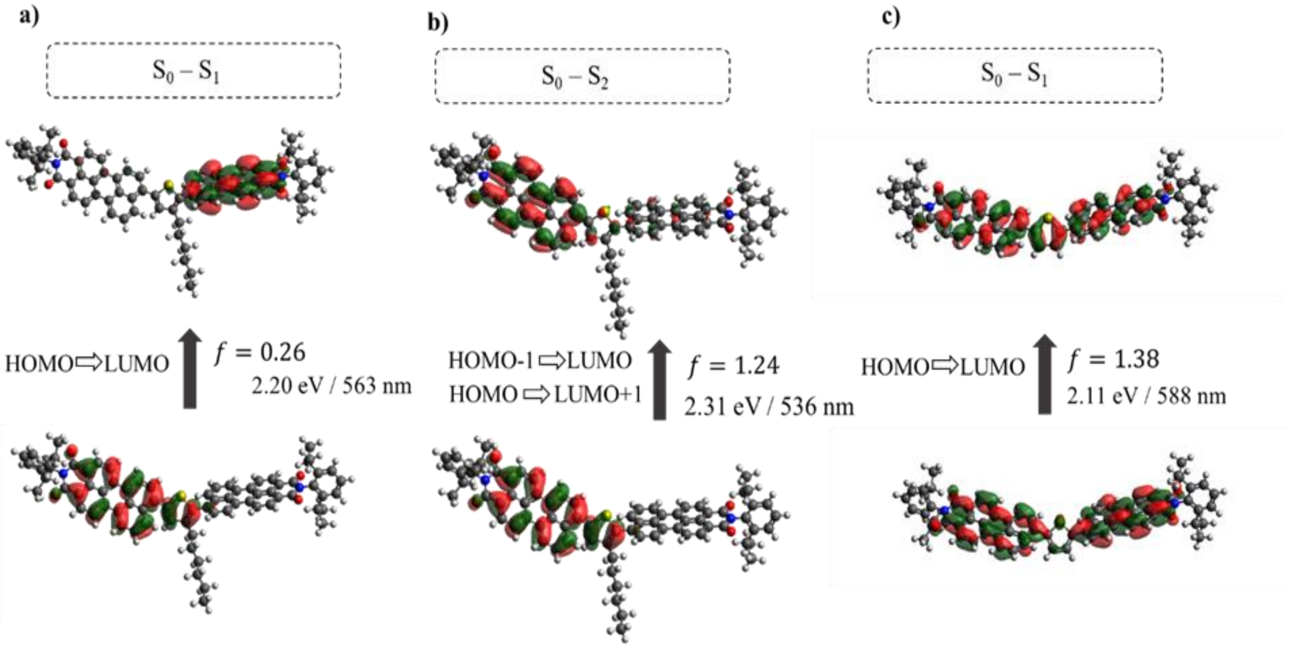

Figure 16. Graphical representation of the HOMO/LUMO levels. a) transition from $S_0 - S_1$ in PMI-hT-PMI molecule, at an oscillator strength of 0.26, b) transition from $S_0 - S_2$ in the PMI-hT-PMI molecule, at the highest calculated oscillator strength of 1.24, c) transition of $S_0 - S_1$ of the PMI-thio-PMI molecule at the highest calculated oscillator strength of 1.38.

The figure shows, that the HOMO and LUMO energy levels in the hexylthiopene-based compound are not coupled, whereas the thiophene-based compound shows the opposite. The coupling of the HOMO/LUMO levels in PMI-thio-PMI is presumably due to the fact, that the molecule exhibits higher planarity and is less twisted.

4.2. Synthesis of PMI and PMI-Br

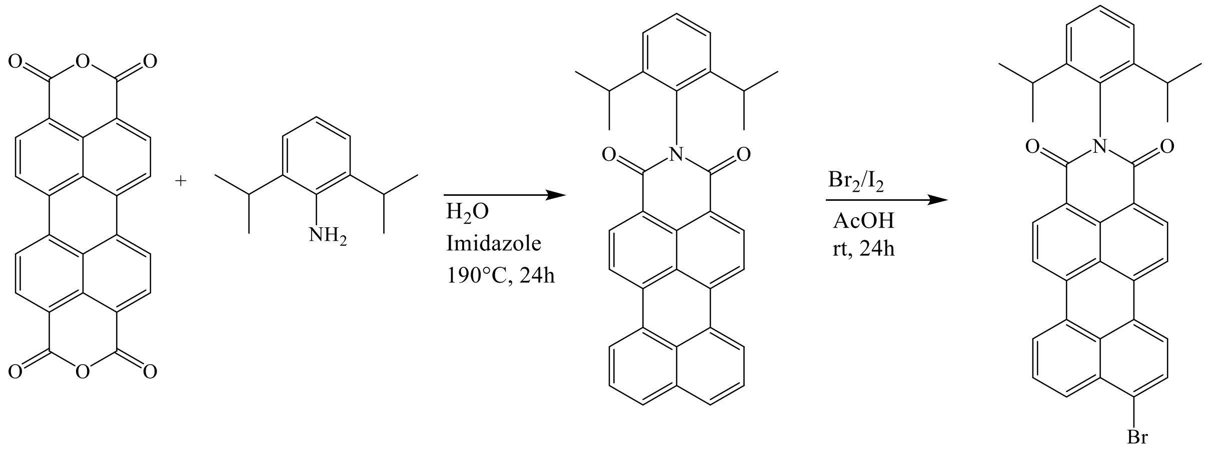

PTCDA **1** **2**

Scheme 1. Overview of the synthesis of perylene monoimide (**1**) and brominated perylene monoimide (**2**).

The building block compound **1** was synthesized according to literature.[73] The starting material perylene-3,4,9,10-tetracarboxylic dianhydride (PTCDA) which is commercially available is suspended in dest. water in presence of the 2,6-diisopropylaniline and imidazole. Due to the fact that the yield increases at higher temperatures than the boiling point of H_2O carried out in closed vessels[73], the reaction was performed in an autoclave at 190 °C.

By decarboxylation on one side of PTCDA and after a reaction time of 24 h, the desired product 1 was obtained in a moderate yield. The complete decarboxylation of the anhydride leads to the formation of the major side product perylene, which can be easily separated by column chromatography. The findings of Langhals et al. revealed that the formation of perylene is favored at higher temperatures, resulting in the determination of 190 °C as the optimum temperature.[73] After cooling down to room temperature, the mixture was acidified up to a pH of 2 with hydrochloric acid. The crude product, isolated by vacuum filtration, is purified afterwards by Soxhlet extraction with chloroform as solvent. Followed by another purification step comprising column chromatography performed again with chloroform.

Next, compound **2** was synthesized by a bromination step according to literature[74], performed in acetic acid as solvent at room temperature for 24h. Therefore 4 equivalents of Br_2 were added together with 0.4 equivalents of I_2 and the reaction was carried out under light exclusion. In this reaction, iodine acts as an effective catalyst and the molar amount of I_2 necessarily needs to be lower than the amount of Br_2 in order to get high reaction rates, as the results from literature reveal.[75]

The work-up includes flushing with N_2 gas for 30 minutes to remove the excess of bromine and dilution in methanol, washing with water until its filtrate is neutral. The red solid was isolated by filtration in vacuo and further drying over NaOH in a desiccator gave the product in a quantitative yield.

4.3. Optimization of Suzuki coupling reaction

Starting from the brominated perylene monoimide (PMI-Br), the linked acceptor molecules are generally synthesized by adding the corresponding organoboron compound via Suzuki coupling.

In order to minimize the side-products, an optimization of the reaction conditions was done. Therefore, different parameters including temperature, duration, sort of base and additives were varied regarding the reaction depicted in Scheme 2, where the thiophene boronic pinacol ester (compound **3**) was coupled with PMI-Br. In this experiment, $Pd(PPh_3)_4$ was used as catalyst in an amount of 5 mol% and toluene was used as the solvent. The reaction approach was done under inert conditions (N_2)

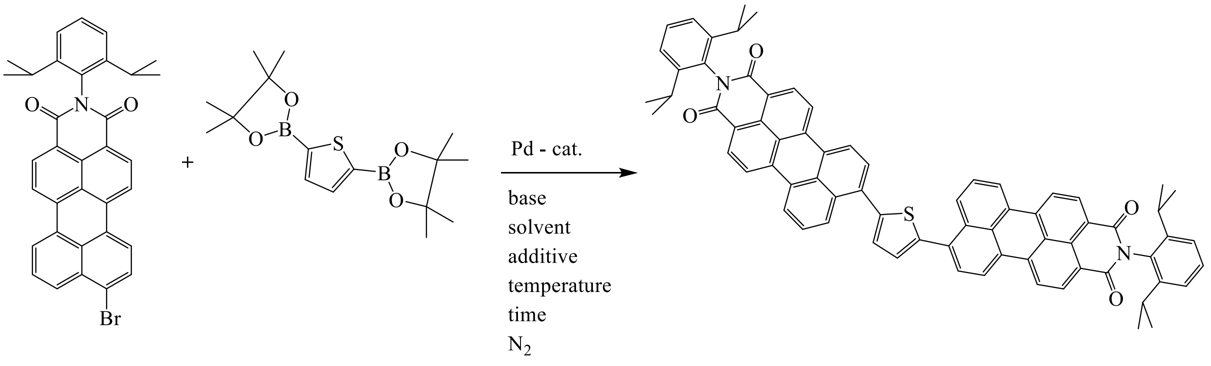

2 : PMI-Br **3: thio(BPn)** **4: PMI-thio-PMI**

Scheme 2. General reaction of Suzuki coupling used for the optimization approach.

The different reaction conditions are summarized in Table 2. The reactions were performed in a heated synthesis reactor by Anton Paar, which enabled shorter reaction time compared to traditional heating plates.

During this experiment, a sample of each crude reaction mixture was taken after a certain period of time as a reaction control procedure. The work-up of the sample comprise washing with dest. H_2O and extraction of the formed products in methylene chloride. The reaction control of each condition (A-E, see Figure 17) was examined by thin layer chromatography and the results of the qualitative investigation towards the formation of side-products were compared. The schematic drawing of the TLC plate is depicted in Figure 17, showing the qualitative analysis of the optimization. The side products are shown in different colors and the product spot is indicated by an arrow with the respective retention factor (Rf). The compound **2** (PMI-Br) was added in excess (ratio of **2**:**3** was 2.2:1). Therefore, the spot appearing on the very top of the plate, eluting the fastest, represents the surplus starting material PMI-Br.

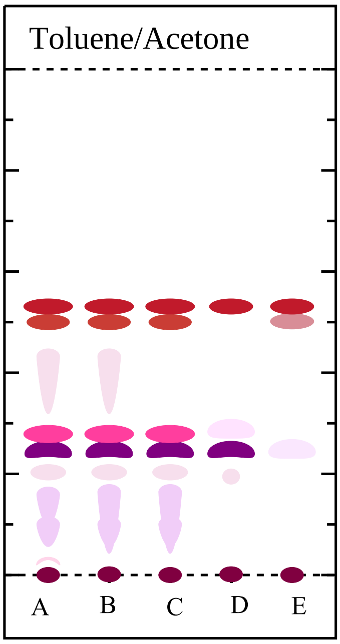

Table 2. Summary of the different conditions used in Suzuki coupling reaction.

Entry	Temp [°C]	Time	Suzuki-Base	Additive
A	110	4 d	Aqueous K_2CO_3 (1 M)	No
B	80	2 h	Aqueous K_2CO_3 (1 M)	No
C	110	2 h	Aqueous K_2CO_3 (1 M)	EtOH
D	110	2 h	Aqueous KF (1 M)	EtOH
E	110	2 h	Dicyclohexylamine	EtOH

Figure 17. Schematic drawing of the TLC plate regarding the qualitative investigation towards side products in Suzuki coupling reaction.

The results reveal that the most side-products were formed when performing the reaction for four days, with aqueous potassium carbonate and no additive (entry A). The addition of ethanol results in a reduction of side products, as seen in entry C,D and E. Moreover, the exchange of potassium carbonate by potassium fluoride as base component also had a beneficial effect on the reaction. The reaction containing dicyclohexylamine as base had a much lower reaction rate and led to nearly no conversion to the desired product. In conclusion, the best result was obtained by using entry D.

The beneficial influence of ethanol, used as an additional solvent in Suzuki coupling reactions, was previously investigated and the results of this optimization experiment are in accordance with literature.[76] The efficiency of ethanol may rely on accelerated reduction of Pd(2+) to Pd(0) (see 2.7), based on assumptions in literature.[77]

Moreover, N. Miyaura reported in his studies on base-assisted Suzuki cross-coupling reactions[78] that the base accelerates the transmetallation step, depicted in Chapter 2.7. The choice of a suitable base is of great importance and plays a key role in cross-coupling reactions. For the reaction depicted in Scheme 2, the results reveal that the most suitable base is potassium fluoride.

4.4. Synthesis of thiophene-linked perylene monoimide compounds (PMI-thio-PMI, PMI-ht-PMI)

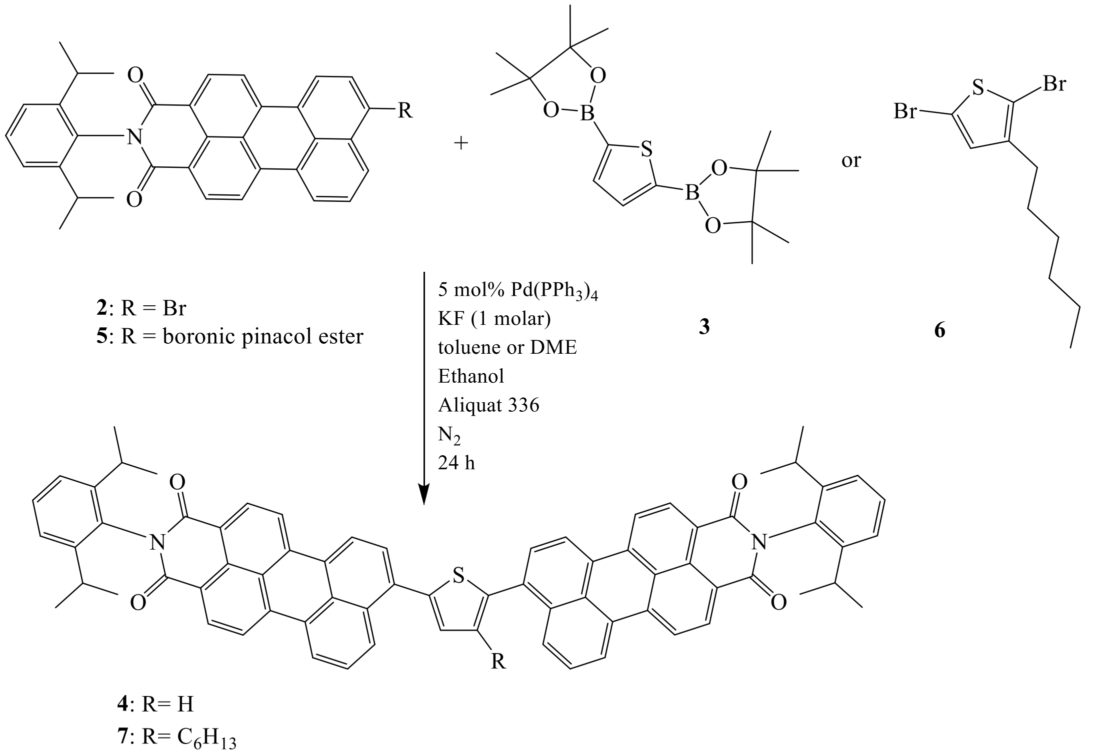

Scheme 3. General scheme of Suzuki coupling reaction towards thiophene-based acceptor molecules **4** and **5**.

The synthesis towards the desired compounds **4** and **7** were carried out following the reaction depicted in Scheme 3. Therefore, an excess of the brominated perylene monoimide PMI-Br was suspended in either toluene or dimethoxyethane (DME) and the thiophene-based boronic pinacol esters were added under inert conditions. The reaction temperatures were adapted to the boiling points of toluene and dimethoxyethane, respectively (110 °C and 85 °C). In order to enable a contact between the basic aqueous layer and the organic layer, Aliquat 336 was used as a phase-transfer catalyst, accelerating the reaction rate.[79]

The first reaction performed was the synthesis of compound **4**. For first approaches, toluene was chosen as solvent and **2** (halide derivative) and the compound **3** were mixed. The work-up consisted of an extraction step in a separation funnel with toluene/H_2O, and the drying of the organic phase over Na_2SO_4. The reaction gave PMI-thio-PMI (**4**) in a moderate yield of 30-40%. During the reaction, a color change from red to violet could be observed, indicating a conversion of the starting materials. Reaction control by thin layer chromatography with toluene and acetone in a ratio of 99:1 as an eluent mixture revealed that some side-products were formed. The side-products eluting much faster or slower than the desired product, having a sufficient distance to the retention factor of **4** on the TLC plate, could be eliminated by column chromatography. However, the purified product still revealed impurities when recording ^{1}H-NMR spectra. PMI-thio-PMI is moderately soluble in common solvents like methylene chloride, toluene, cyclohexane or chloroform, hence impeding the purification steps. Also, recrystallization was not successful, due to solubility issues.

Since a similar thiophene-based compound is reported in literature[39], the aromatic region was compared. The results are shown graphically in Figure 18.

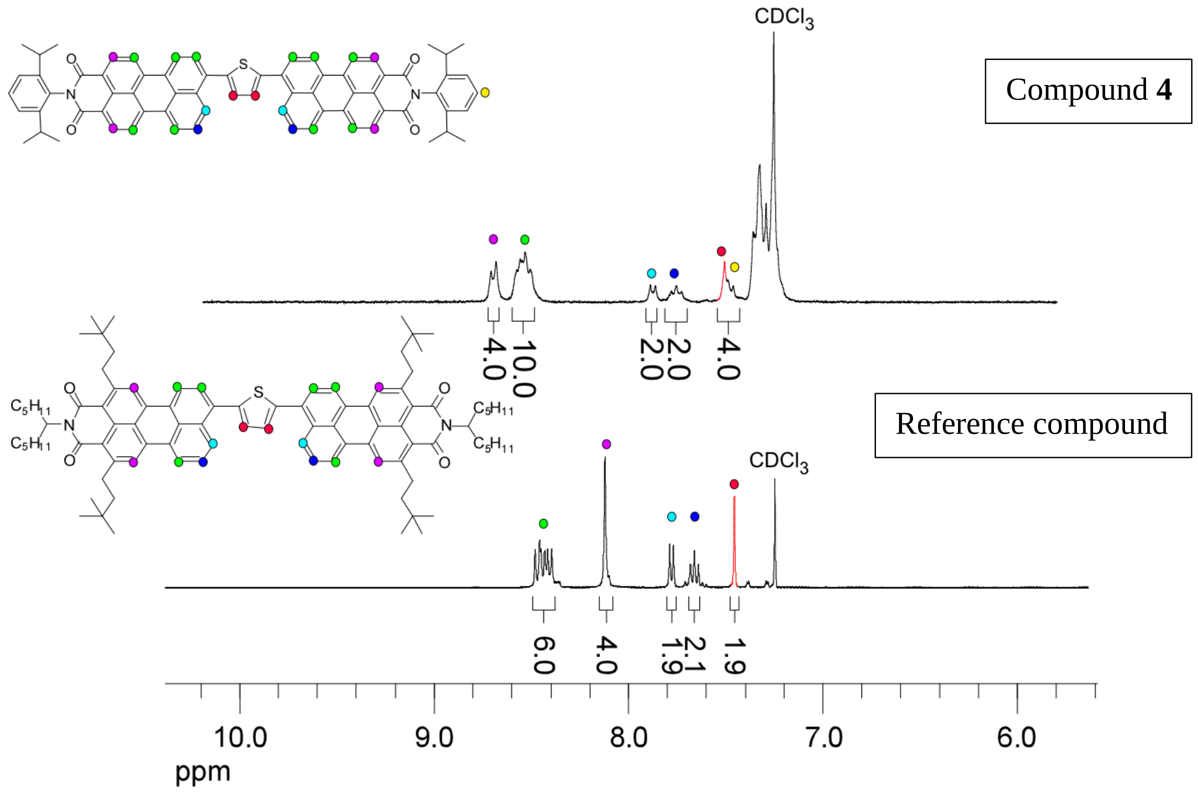

Figure 18. Comparison of the aromatic (^{1}H-NMR) of the reported product and compound 4. The colored dots indicate the corresponding proton peaks in the spectra. Illustration was made by Matiss Reinfelds. Adapted with permission from Hu, Y.; Chen, S.; Zhang, L.; Zhang, Y.; Yuan, Z.; Zhao, X.; Chen, Y. *J. Org. Chem.* 2017, 82 (11), 5926-5931. Copyright 2020 American Chemical Society.

The ^{1}H-NMR spectrum of the reference compound shows shifted values in the region 8.4 – 8.6 ppm, which is due to the additional alkyl-chains on the perylenemonoimide core (greed dots in Figure 18). However, the proton signals coming from the thiophene-linker are in accordance with literature (7.52 ppm in compound **4**, versus 7.45 ppm in reference compound). Moreover, the proton signal of the thiophene is overlapping with the protons from diisopropylaniline (yellow dots in Figure 18).

For the synthesis of compound **7**, the halide comprised of compound **6**. Compound **5**, constituting the organoboron substrate, was not part of this work and was provided by Matīss Reinfelds. In contrast to PMI-Br, **5** is much more soluble in the used solvents (toluene and DME). Herein, a color change was observed during the reaction from red to purple. The work-up is the same as before and the reaction gave **7** in a moderate yield of 30-45%. Contrary to the first product, compound **7** shows excellent solubility in common organic solvents like toluene, chloroform and methylene chloride. This can be attributed to the substitution of a hydrogen on the thiophene by a hexyl chain, which hinders the aggregation. For that reason, purification by column chromatography and recrystallization from CH_2Cl_2/methanol was successful.

As it is reported in literature, hydrolytic protodeboronation and homocoupling are two reaction that are competing with the main Suzuki-coupling pathway.[80] The possibility of protodeboronation is increased, since this side-reaction occurs especially in aqueous media and herein, concerning the reaction in Scheme 3, the potassium fluoride is dissolved in H_2O. During this reaction, the boronic compound bound to the aryl is exchange by a proton.

Furthermore, the oxidative homocoupling of two aryl substrates is often observed as a side-reaction in palladium catalyzed cross-coupling reactions, generated from aryl-boronic esters (see Scheme 4).[70]

$$2\ \mathrm{ArB(OR)_2} + \mathrm{OX} \longrightarrow \mathrm{Ar\text{-}Ar} + \mathrm{Red} + 2\ \text{"}\mathrm{B(OR)_2}\text{"}$$

Scheme 4. General reaction equation of oxidative homocoupling of two aryl-boronic compounds.

As it is reported in literature, this reaction is catalyzed by pure oxygen or even air.[70] Although the reaction was performed under inert conditions, it is possible that not all of the air/oxygen is excluded, for which reason homocoupling would be possible. This statement is affirmed, since the mass spectrometry measurement of PMI-thio-PMI revealed besides the main molecular ion signal at 1042.4 a second $[M]^+$ ion signal at 1124. The difference accounts for 82, which indicated another thiophene, linked to the PMI-thio-PMI. This side-product could have been formed by oxidative homocoupling of two the thiophene-boronic pinacol ester moieties. The MS spectra are included in the appendix.

Compound **5** was furthermore synthesized including dimethoxythane as solvent, in which the starting materials are also good soluble. This approach changed in terms of the work-up process. Due to the fact, that DME is miscible in H_2O, the solvent had to be removed under reduced pressure in a rotary evaporator, before performing the extraction step with toluene/H_2O. Purification was done again with column chromatography, as described in the first approach. The results differ only regarding the purification by recrystallization. In this regard, less recrystallization steps were necessary to remove the side-products, compared to the synthesis performed in toluene as solvent.

The NMR spectra of **4** and **7** were recorded in deuterochloroform and are included in the appendix.

4.5. Synthesis of the tetraphenylethylene-linked PMI compound (PMI$_4$TPE)

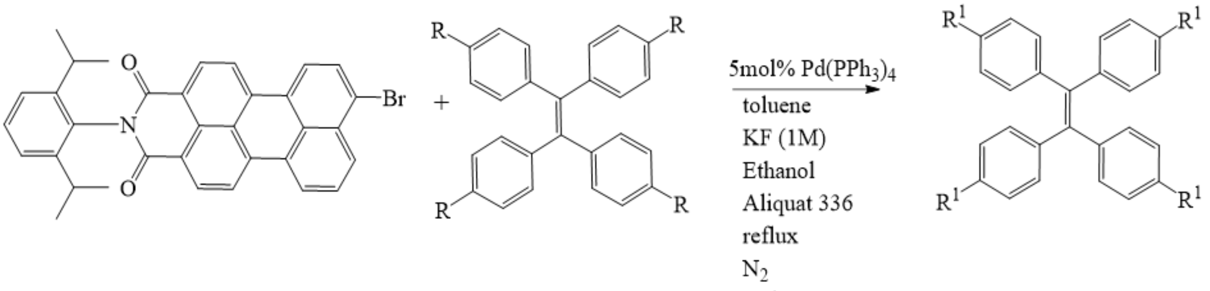

2: PMI-Br **8**: R = boronic pinacol ester **9**: R^1 = PMI

Scheme 5. Synthesis (PMI)$_4$TPE via Suzuki-coupling.

In order to synthesize compound **9**, the substrates **2** and **8** were suspended in toluene under inert conditions. The conditions are again the same as in 4.4. PMI-Br was added in an excess amount and the ratio of the halide to the compound **7** is 8:1 in order to drive the reaction towards completion. Since the coupling happens in this case four times, the reaction time was extended in comparison to Scheme 3. (varying between 24 h and 72 h). In order to bring the reaction to a complete conversion another 5 mol% of the catalyst were added after 24 h. However, this did not change the outcome of the Suzuki-coupling. Purification by column chromatography with different eluents was moderately successful, due to the small difference in retention factors of the products formed. Therefore, a pure product was not achieved and for time reasons, no further purification was done.

During this reaction, many side-products are formed, which were determined by TLC. The formation of mono-, bis-, or tris-coupling of the perylene monoimide moiety to the tetraphenylethylene-linker is presumably occurring.

The findings of Sinclair D. J. and Sherburn M. S. show, that coupling is mostly depending on the halide nature and is rather weakly influenced by different conditions concerning base, solvent and temperature. Their results demonstrate clearly that the selectivity between mono and di-coupling is based on the used halide, whereas di-coupling is more favored using iodine as leaving group and mono-coupling with bromide compounds.[81] This fact is presumed to be the reason for such low conversions towards the quadrupol-coupled compound **9** depicted in Scheme 5.

4.6. Optical properties of PMI-thio-PMI and PMI-ht-PMI

In order to characterize the thiophene-linked PMI compounds, absorption spectra were recorded, with chloroform as solvent. As the concentration of the solutions and the absorbance was known, the molar absorption coefficient was determined. The absorption spectra are depicted in Figure 19.

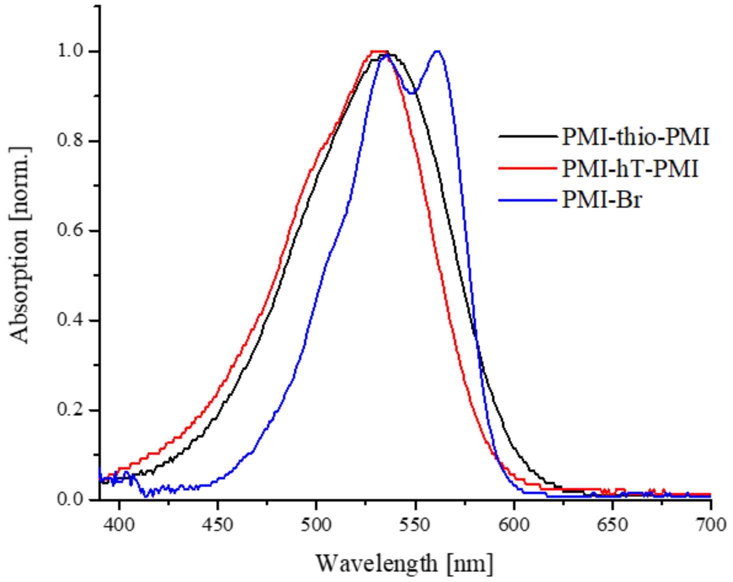

Figure 19. Absorption spectra of the thiophene-linked PMI compounds and the starting material PMI-Br recorded in $CHCl_3$.

The maximum absorbance of PMI-hT-PMI appears at 536 nm and the maximum of PMI-thio-PMI is at 531 nm. As expected, the absorption range is not heavily influenced by the hexyl chain included in PMI-hT-PMI, resulting in very similar absorption maxima with a shift of the wavelength of 5 nm. Compared to the absorption maximum of the educt PMI-Br, which appears at 561 nm, the absorptions of the linked-PMI compounds are slightly blue-shifted. Moreover, the brominated PMI shows a second absorption maximum at 536 nm.

By using the Lambert-Beer law, the molar absorption coefficient (ε) can be determined for the three samples. The building block compound PMI-Br exhibits a molar absorption coefficient of 30 500 L mol^{-1} cm^{1}, which is the lowest value. The thiophene-linked compound PMI-thio-PMI exhibits the highest and nearly four-times higher value of 125 900 L mol^{-1} cm^{1} compared to the educt, and the hexylthiophene-linked compound shows a molar absorption coefficient of 71 600 mol^{-1} cm^{1}. Since the only difference between these two molecules is the hexyl-chain, similar values of the absorption coefficient were expected. Therefore, it is assumed, that the PMI-thio-PMI shows higher values, due to impurities.

Furthermore, the optical bang gap (E_G^{opt}) was determined graphically for PMI-Br, PMI-thio-PMI and PMI-hT-PMI, by using the UV-Vis spectra. Therefore, a tangent was plotted towards that point, where the absorption peak flattens out. The values for the optical bang gap were summarized in Table 3.

Table 3. Determination of the optical band gap experimentally by UV-Vis spectra and by DFT calculations.

Compound	$\mathbf{E_G^{opt}}$ [eV] by UV-Vis	$\mathbf{E_G^{opt}}$ [eV] by DFT/6-31+G (d, p)	$\mathbf{E_G^{opt}}$ [eV] by DFT/6-31G (d, p)
PMI-Br	2.29	-	-
PMI-thio-PMI	2.06	2.11	2.17
PMI-hT-PMI	2.11	2.20	2.26

Concerning the non-diffuse basis set 6-31G (d, p), the E_G^{opt} value for PMI-thio-PMI is 2.43 eV and about 15% higher, related to the experimentally determined value of 2.06 eV. The diffuse basis set is slightly more in accordance to the value of 2.06 eV. Concerning PMI-hT-PMI, the value calculated by the non-diffuse basis set, is 17% higher than the experimentally determined band gap of 2.11 eV.

Moreover, fluorescence spectra were recorded for PMI-hT-PMI and PMI-thio-PMI in $CHCl_3$ and the relative quantum yield (Φ) was calculated, taking into account the refractive index of the solvent, absorption and emission of the sample and the reference material ('Lumineszenzorange' with a quantum yield of >90%[82]). The absorption and emission spectra of the samples are depicted in Figure 20.

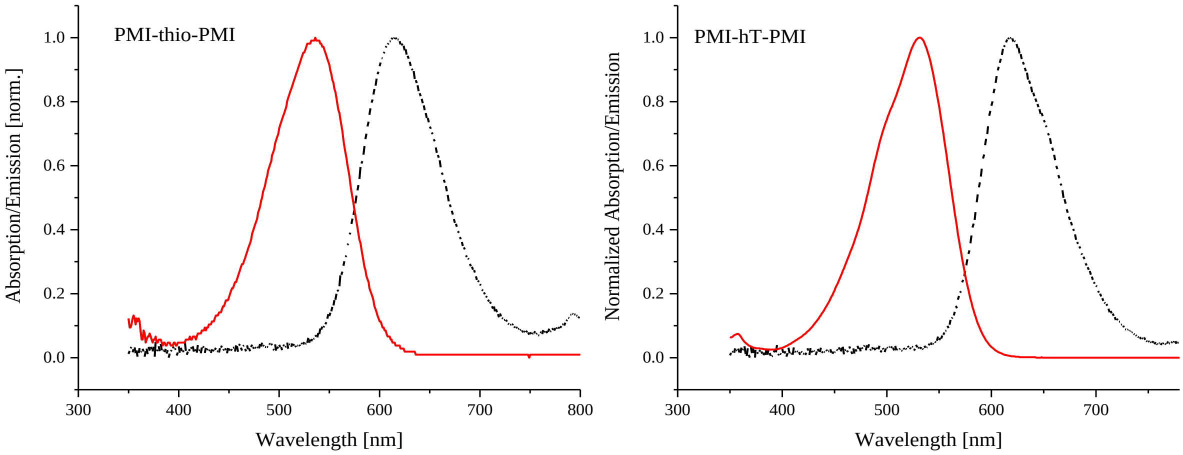

Figure 20. Absorption (red line) and emission (dashed line) spectra of PMI-hT-PMI and PMI-thio-PMI.

PMI-hT-PMI shows a stokes shift of 88 nm, which is comparable to the value for PMI-thio-PMI of 80 nm. The calculated quantum yields are summarized in Table 4, consisting of average values of three measurements.

Table 4. Relative quantum yield Φ calculated using the absorption and emission spectra of the compounds and the reference.

Compound	**Relative quantum yield Φ** [%]
PMI-thio-PMI	47.2
PMI-hT-PMI	55.0

4.7. Organic Solar Cells

The assembly of the solar cells and the respective energy diagram[83,84] are depicted in Figure 21, consisting of a bulk heterojunction and inverted device design. The inverted design attributes the ITO layer as the anode (ZnO as the electron transport layer) and silver as the cathode (MoO_3 as hole transport layer). The general production procedure includes deposition of the interfacial ZnO layer by sol-gel technique onto the glass/ITO substrates, followed by the depositions of the active layer, diluted in chlorobenzene, and the thermal evaporation of MoO_3 and Ag, as another interfacial layer and the cathode, respectively. Further description of the production procedure is declared in Chapter 6.3.1.

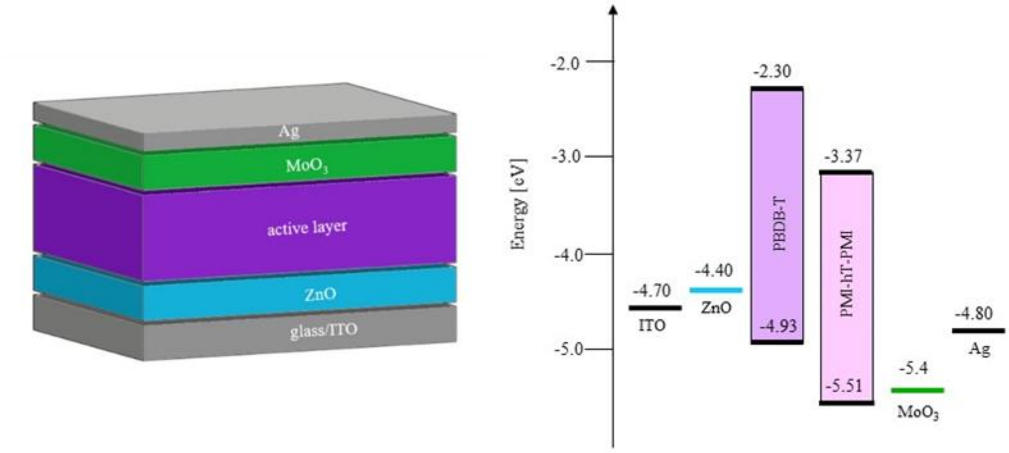

Figure 21. Schematic depiction of the solar cell devices with inverted structure and the respective energy diagrams of ITO, ZnO, donor, acceptor and MoO_3.

As the acceptor material, the synthesized hexyl-thiophene-based compound PMI-hT-PMI was used in combination with PBDB-T (PCE-12) as the donor material (see Figure 22). Since the donor material exhibits higher lying HOMO and LUMO levels, as it is shown in the energy diagram in Figure 22, it possesses appropriate energy levels related to the acceptor and an exciton dissociation is enabled.

In order to investigate the influence of the donor/acceptor ratio, two approaches were done. Firstly, a ratio of D/A of 1/1 was examined, and secondly a ratio of 1/0.5.

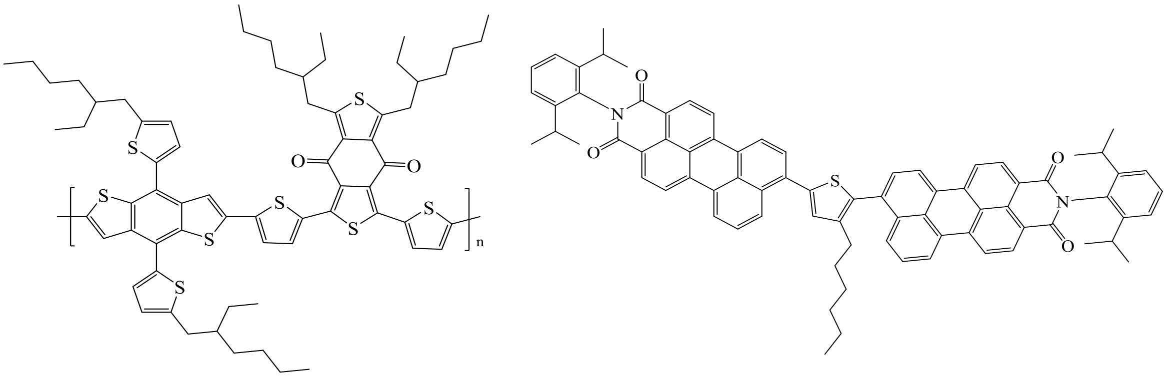

Figure 22. Donor (left, PCE-12) and acceptor (right, PMI-hT-PMI) material used in the solar cell devices.

4.7.1. Solar cells with a donor/acceptor ratio of 1/1

Herein, the acceptor was dissolved in chlorobenzene in a concentration of 10 mg/mL, whereas the donor was dissolved in the same concentration. The mixture of donor and acceptor were spin coated on the substrates, with a speed of 2000 rmp, resulting in an average layer thickness of 55.7 nm ± 1.21 nm (average of 10 substrates). The roughness of the active layer was rather low with average values of 1.71 nm ± 0.467 nm. Therefore, it is assumed, that the layer on the substrate was quite homogeneously distributed and show smooth surfaces, which is beneficial for functioning in solar cells. As it is reported in literature[85], the short-circuit current and fill factor are increased with smoother surfaces. Since the formation of clusters and phase-separation occurs in rougher film-layers, the charge carrier mobility is decreased, leading to lower currents and FF values.[85] Moreover, smooth surfaces assure a good contact between the active layer and the top electrode.[86]

The UV-Vis absorption spectra measured on thin films are depicted in Figure 23. In order to investigate the development of the photovoltaic parameters upon temperature, first optimization attempts were performed towards an annealing treatment.

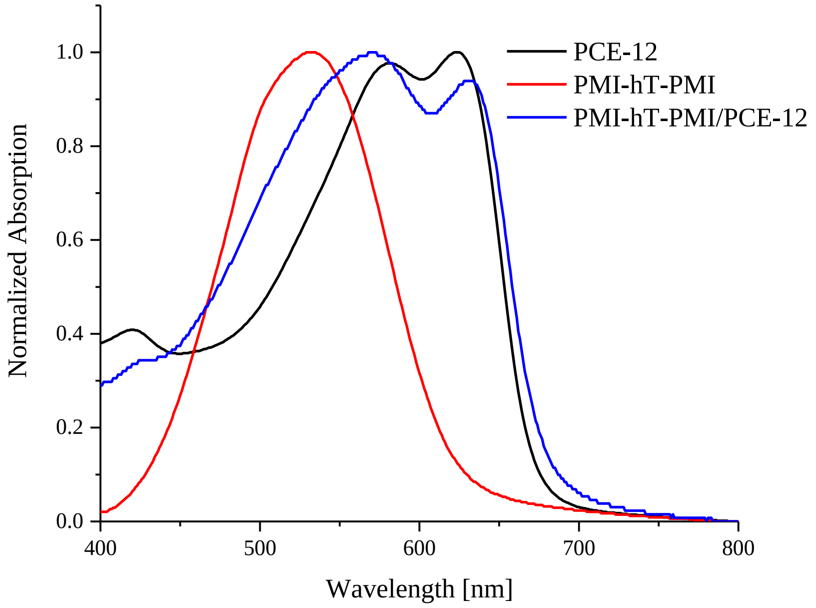

Figure 23. Absorption spectra of the neat acceptor (PMI-hT-PMI, red curve), donor (PCE-12, black curve) and the blend in D/A ratio of 1/1 (blue curve), all recorded on films

4.7.1.1. Influence of annealing on solar cells with D/A ratio of 1/1

In the first attempt the samples containing a D/A ratio of 1/1 were annealed at a certain temperature, followed by the measurement of the J-V characteristics and the average values of 8 substrates were calculated. The temperature values were selected from 80 °C up to 200 °C and the substrates were heated on a conventional heating plate in the glove box each for 10 minutes. In addition, a measurement at room temperature (25 °C) was performed, without an annealing step. The results of this experiment are summarized in Table 5.

Table 5. I-V characteristics of the solar cells with a D/A ratio of 1/1 with the respective annealing temperature. The average values of the best 8 cells for each temperature are given with their respective standard deviation.

Temp. [°C]	**V_{oc} [V]**	**J_{sc} [mA/cm^2]**	**FF [%]**	**PCE [%]**
25	1.07 ± 0.04	-7.70 ± 0.52	33.4 ± 1.58	1.92 ± 0.22
80	1.06 ± 0.02	-8.68 ± 0.30	35.7 ± 0.91	2.27 ± 0.16
100	1.04 ± 0.01	-8.96 ± 0.24	36.9 ± 0.42	2.42 ± 0.11
120	1.06 ± 0.01	-9.20 ± 0.22	37.9 ± 0.77	2.57 ± 0.11
140	0.98 ± 0.03	-8.76 ± 0.56	39.8 ± 1.23	2.39 ± 0.30
160	1.00 ± 0.02	-8.83 ± 0.28	39.3 ± 0.93	2.41 ± 0.14
180	0.96 ± 0.02	-8.69 ± 0.44	39.3 ± 1.70	2.29 ± 0.29
200	0.89 ± 0.06	-9.98 ± 0.37	41.0 ± 1.55	2.55 ± 0.23

When discussing the results, it has to be taken into account that the actual temperatures supplied by the used heating plate are about 20 °C lower than indicated.

The results show that the lowest values are obtained when no annealing step is performed. On the other hand, the best values with a power conversion efficiency of 2.57%, V_{oc} of 1.06 V, J_{sc} of -9.20 mA/cm^2 and a fill factor of 37.9% were obtained with an annealing temperature of 120 °C. Figure 24 shows the variations of the solar cell characteristics as a function of temperature. Therefore, the average values of FF, PCE, V_{oc} and J_{sc} were plotted against the annealing temperature with the respective standard deviation.

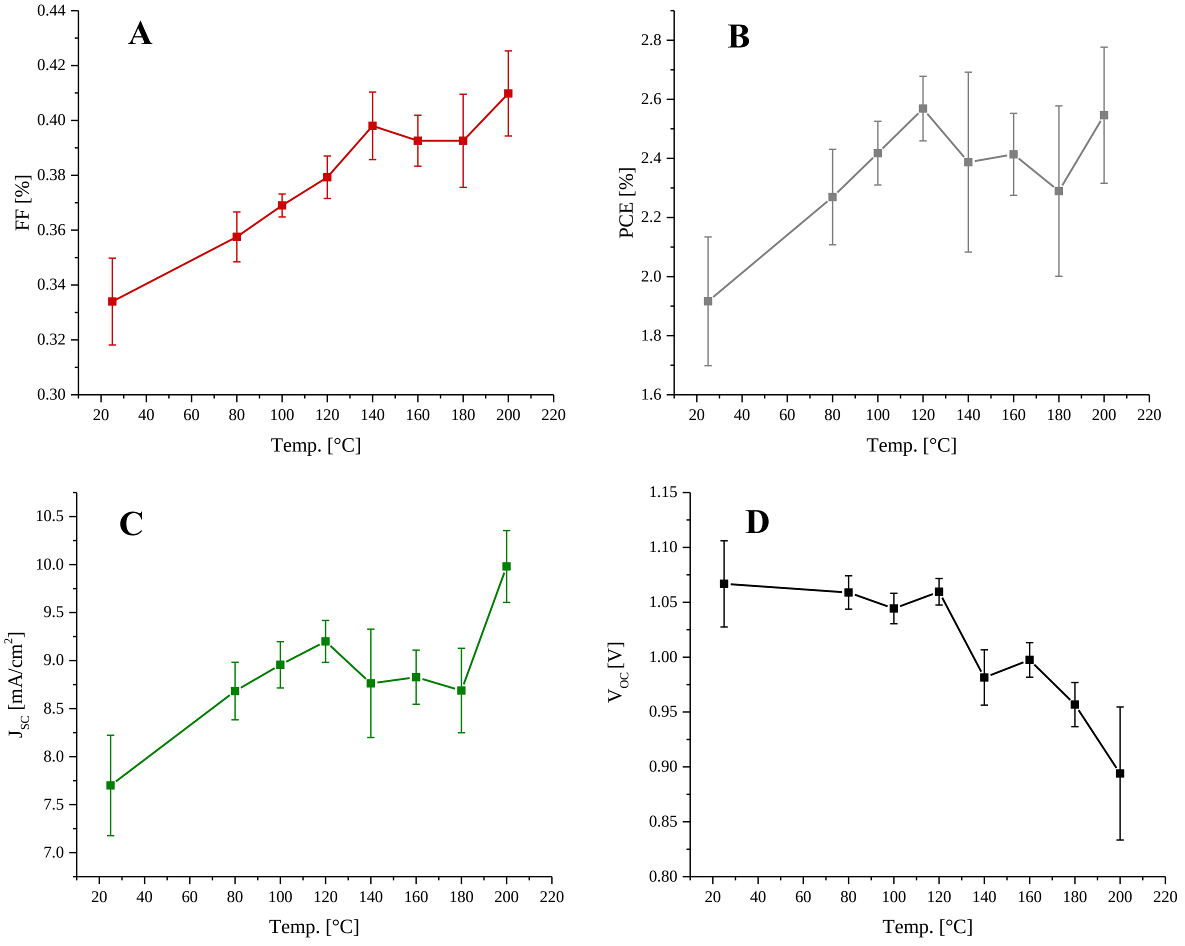

Figure 24. Average values and respective standard deviations of fill factor (**A**), power conversion efficiencies (**B**), current density (**C)** and open-circuit voltage (**D**) plotted against the annealing temperature.

Figure 24/B shows the efficiency rises initially upon annealing, reaching a maximum at 120 °C. Above this temperature, no significant changes are observable until 200 °C and the PCE ranges from 2.2. to 2.7%. The current density depicted in Figure 24/C, is the highest at 200°C and is in general steadily increasing with higher temperatures.

The fill factor (A) shows also a significant overall-increase upon annealing. While the FF displays values of values of 33% with a corresponding J_{sc} of -7.70 mA/cm^2 at room temperature, these J-V characteristics show an improvement at moderate temperatures of 120 °C. At this temperature, J_{sc} increases to -9.20 mA/cm^2 and the FF to 38%.

Moreover, temperatures of 200 °C induce another distinct increase of these two values to -9.98 mA/cm^2 and 41%. However, the standard deviation needs to be considered, leading to no proper statement, especially for the J_{sc} value at 140 °C, ranging from -8.20 mA/cm^2 to -9.32 mA/cm^2. Concerning the open-circuit voltage, depicted in Figure 24/D, it nearly stays the same below 120°C, followed by a decline above 120 °C.

As it is reported in literature, annealing treatments induce a crystallization process in the organic layers and lead to an improved morphology. As the materials get more crystalline, charge transport to the electrodes is facilitated, resulting in a beneficial improvement of the J-V characteristics of organic solar cells.[87,88] Yang X. et al. also observed an significant improvement of the fill factor and short-circuit current with higher annealing temperature, related to organic solar cells with a P3HT:PCBM blend as the active layer . The improvement of the FF and J_{sc} is resulting from decreasing serial resistances, which is again based on the better crystallinity of the materials.[87] Chen et al. observed the improvement by annealing with BHJ organic solar cells containing the same donor as in this work, PBDB-T. Their findings reveal an increase in FF and current density, resulting from increased hole and electron mobilities and enhanced external quantum efficiencies.[86] The J-V curve of the best cell is depicted in Figure 25 and the respective solar cell parameters are summarized in

.

V_{oc} [V]	**J_{sc} [mA/cm^2]**	**FF [%]**	**PCE [%]**
1.08	-8.05	38.4	3.35

Conditions

- Annealing at 120°C for 10 min.
- Storage in glove box for 48h
- Light-soaking for 10 min.

In Figure 25 the black line indicates the measurement under dark conditions, whereas the red line shows the measurement under illumination. This cell was initially prepared including an annealing step under 120°C for 10 minutes, resulting in a power conversion efficiency of 2.90%, V_{oc} of 1.08 V, J_{sc} of -7.12 mA/cm^2 and FF of 38.7%. After a storage time of 48h in the glove box, not excluding light, the cell showed an increase in PCE of 12%, exhibiting a PCE value of 3.29%. Finally, after light-soaking for 10 minutes, the PCE was again slightly increased up to 3.35%, with a V_{oc} of 1.08 V, J_{sc} of -8.05 mA/cm^2 and a fill factor of 38.4%.

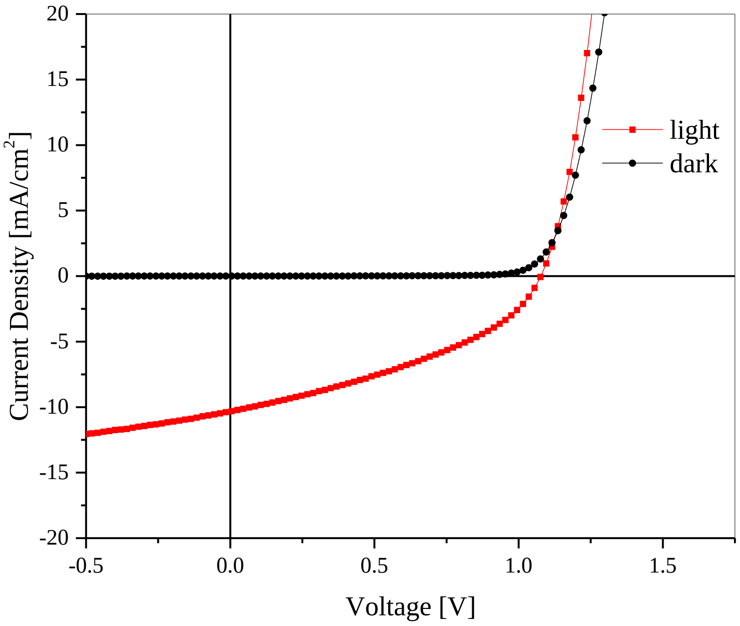

Figure 25. J-V characteristics of the best solar cell containing PCE-12/ PMI-hT-PMI in a ratio 1/1 as active layer.

Table 6. Solar cell parameters of the best cell and the respective conditions

V_{oc} [V]	**J_{sc} [mA/cm^2]**	**FF [%]**	**PCE [%]**
1.08	-8.05	38.4	3.35

Conditions

- Annealing at 120°C for 10 min.
- Storage in glove box for 48h
- Light-soaking for 10 min.

In addition to the J-V characteristics, light microscope images were recorded of the substrates, annealed at different temperatures, with a light microscope in a magnification of 500x (see Figure 26).

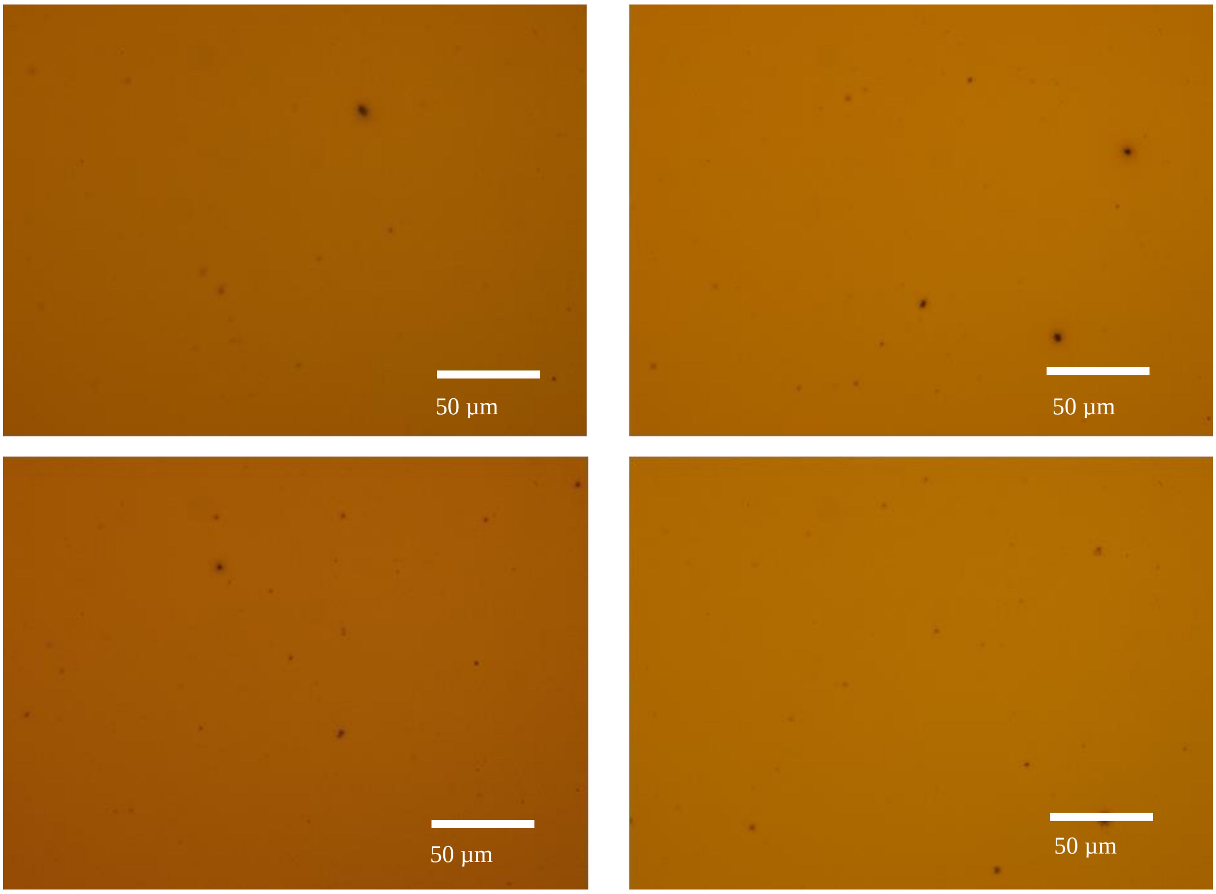

Figure 26. Images of the active layer recorded with light microscopy with a magnitude of 500x and a donor/acceptor ratio of 1/1. Upper row: no annealing treatment (left), annealing temp. of 120 °C (right). Lower row: annealing temp. of 160 °C (left), annealing temp. of 200 °C (right).

The images show, that the spin-coating process of the donor/acceptor blend creates quite smooth surfaces, with only few dust particles. Moreover, the surface structure exhibits no further modification induced by annealing treatments at temperatures of 120 °C, 160 °C and 200 °C. The thickness, resulting from a spin-coating speed of 2000 rpm of the substrates is 55.7 nm ± 1.21 nm.

4.7.1.2. *Maximum Power point tracking*

In order to examine the long-term stability of the solar cells, a maximum power point (mpp) tracking experiment was performed under inert conditions. Therefore, a solar cell with D/A ratio of 1/1 was illuminated with white light from a LED lamp, in order to avoid heating effects, for 66 h whereas the J-V characteristics were measured simultaneously.

The mpp tracking is depicted in Figure 27 and shows the temporal evolution of the power conversion efficiency.

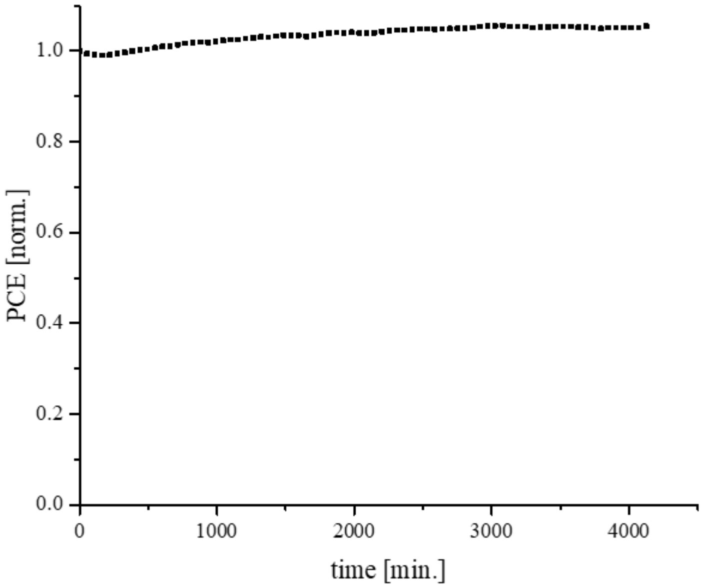

Figure 27. Maximum power point tracking of a solar cell containing a donor/acceptor ratio of 1/1, showing the normalized power conversion efficiency as a function of time.

The power conversion efficiency at the beginning of the experiment was normalized to 1. The results reveal that after three hours, the PCE value is decreasing by 1.1% compared to the point at time zero, followed by a gradually increase until the end of the experiment, after 4000 h light exposure.

After half-time, the PCE has increase by 4% and in the end, an overall-increase of 6% is determined. By this experiment, photo-stability can be assigned as a property for the bulk heterojunction organic solar cells based on PMI-hT-PMI/PCE-12.

At this point, it needs to be mentioned that performance loss is observed in organic photovoltaics over long periods of time.[89] These degradation issues include a steep initial degradation within 70 hours, whereas the largest changes occur within 24h, referred to photoinduced "burn-in", when exposed to light under inert conditions.[90] Such BHJ organic solar cell devices experience an exponential decay in efficiency within this time range. Depending on the materials used in the system, losses range between 10-50%. Especially in fullerene-based BHJ OSCs this effect occurs and as it is reported in literature[89], it results from the formation of oligomers which is not advantageous for the electronic properties. The photo-induced degradation is happening in the photo-active layer and is independent of the electrode materials.[91] Recently, the working group of C. J. Brabec investigated a burn-in free BHJ OSC device, based on a non-fullerene acceptor, which does not show the typical exponential decay in efficiency.

Since the severe “burn-in” effects occur already during the first 24 hours, it can be observed in Figure 27 that the device efficiency is not exponentially decreased. The PCE has even increased by 6%, which would also indicate a “burn-in” free system.

In addition, the solar cell characteristics were measured directly after production, before and after mpp tracking. The results are summarized in Table 7.

Table 7. Photovoltaic characteristics of a single solar cell with a D/A ratio of 1/1. Point zero indicates the results of the measurement directly after production.

Measurement No.	Point in time [h]	V_{oc} [V]	J_{sc} [mA/cm^2]	FF [%]	PCE [%]
1	0	0.97	-9.63	41.8	2.75
2	168	0.95	-14.8	39.3	3.90
3	234	0.97	-15.8	40.5	4.25

The results show a significant increase at every point of time. Before the second measurement was performed, the solar cell was stored in under inert conditions, without the exclusion of light. Due to this, it can be stated, that even the light-soaking through normal storing conditions (for 168 hours) has a significant beneficial effect on the photovoltaic parameters. Whereas current density and PCE is increasing, the V_{oc} and fill factor are not changing.

4.8.1. Solar cells with a donor/acceptor ratio of 1/0.5

The second series of solar cell devices was assembled with a donor/acceptor blend in a ratio of 1/0.5. Herein, the donor was dissolved in chlorobenzene in a concentration of 10 mg/mL, whereas the acceptor was dissolved in a concentration of 5 mg/mL. In order to get comparable thicknesses, the blend of the active materials was spin-coated with a lower speed of 1500 rpm, since the concentration of the PMI-hT-PMI solution is half as much than in the first experiment. The thickness in the second approach was determined with 73.9 nm ± 6.4 nm.

4.8.1.1. Influence of annealing on solar cells with D/A ratio of 1/0.5

In the second attempt, the solar cells with a D/A ratio of 1/0.5 were annealed at temperatures between 80 °C and 200 °C. The parameters are summarized in Table 8 consisting of average values of the 8 best cells with the respective standard deviation.

The best solar cells exhibit an average power conversion efficiency of 2.24%, with an open-circuit voltage of 1.01 V, an average current density of -7.94 mA/cm^2 and a fill factor of 40.2%. The annealing temperature in this case was 180°C. The behavior of the fill factors, PCE, open-circuit voltages and current densities as a function of the annealing temperature are depicted in Figure 28.

Table 8. I-V characteristics of the solar cells containing D/A ratio of 1/0.5 with the respective annealing temperature. The average of the best 8 cells for each temperature is given with the respective standard deviation.

Temp. [°C]	**V_{oc} [V]**	**J_{sc} [mA/cm^2]**	**FF [%]**	**PCE [%]**
25	1.01 ± 0.01	-5.09 ± 0.21	34.8 ± 0.73	1.25 ± 0.075
80	1.02 ± 0.02	-5.52 ± 0.36	35.5 ± 0.43	1.38 ± 0.12
100	1.03 ± 0.01	-5.92 ± 0.21	36.6 ± 0.79	1.56 ± 0.091
120	1.04 ± 0.01	-6.46 ± 0.41	36.8 ± 0.91	1.71 ± 0.19
140	1.05 ± 0.01	-6.84 ± 0.39	37.6 ± 0.71	1.88 ± 0.17
160	1.04 ± 0.02	-6.77 ± 0.44	37.9 ± 0.46	1.87 ± 0.18
180	1.01 ± 0.02	-7.94 ± 0.64	40.2 ± 2.01	2.24 ± 0.39
200	0.992 ± 0.02	-8.02 ± 0.42	40.2 ± 0.90	2.22 ± 0.22

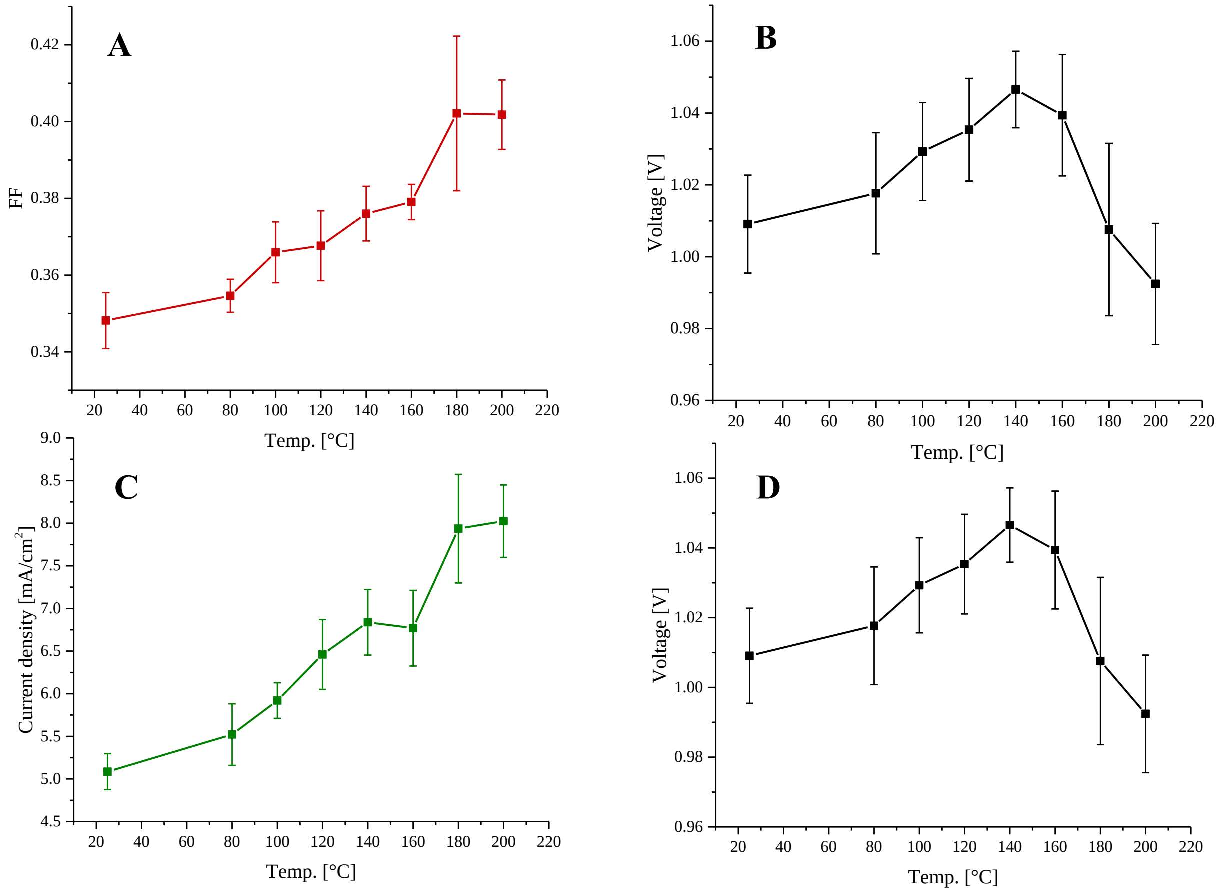

Figure 28. Average values and respective standard deviations of fill factor (**A**), power conversion efficiencies (**B**), current density **(C)** and open-circuit voltage (**D**) plotted against the annealing temperature.

The solar cells clearly show an increase in fill factor, efficiency and current with increasing annealing temperatures. It is the same behavior as observed in chapter 5.6.1. concerning solar cells with a D/A ratio of 1/1. Whereas the voltage is ranging between 0.99 V and 1.04 V, increasing slightly up to 140 °C, followed by a slightly decrease with higher temperatures. Since the FF, PCE and current density increases the most when heating up from 160 °C to 180°C, it can be assumed that annealing in the range of the glass-transition temperature of the donor PCE-12 (about 150°C) is beneficial for the solar cell parameters.

Moreover, the optimum annealing temperature in this case appears to be 180 °C. The J-V curves under light and dark conditions of the best cell are depicted in Figure 29. The photovoltaic parameters are summarized in Table 9, with the respective measurement conditions.

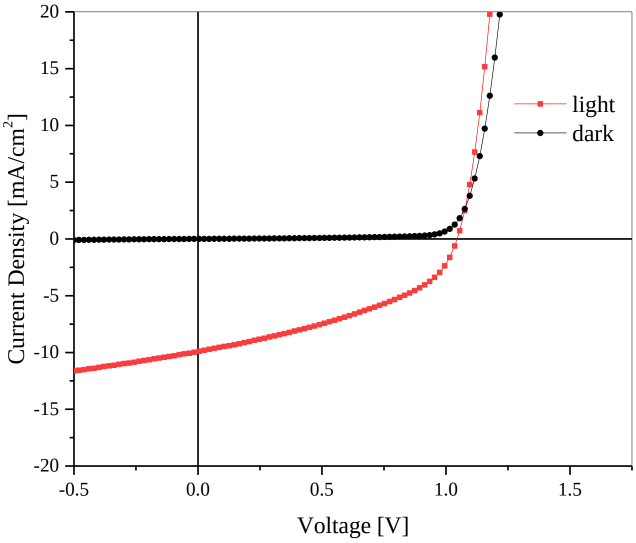

Figure 29. J-V characteristics of the best solar cell containing PCE-12/ PMI-hT-PMI in a ratio 1/0.5 as active layer.

In contrast to the solar cells with a D/A ratio of 1/1, discussed in chapter 0, herein the values of voltage, current and power conversion efficiency are slightly lower, whereas the fill factor is increased. In this case, the best solar cell performance was reached with an annealing treatment at 180 °C (compared to 120 °C in the first series) for 10 minutes.

Table 9. Photovoltaic parameters of the best cell consisting of a D/A ratio of 1/0.5 and the respective conditions.

V_{oc} [V]	J_{sc} [mA/cm^2]	FF [%]	PCE [%]
1.04	-7.72	41.2	3.31

Conditions

- Annealing at 180°C for 10 min.
- Storage in glove box for 48h
- Light-soaking for 10 min.

The respective light microscope images are depicted in Figure 30.

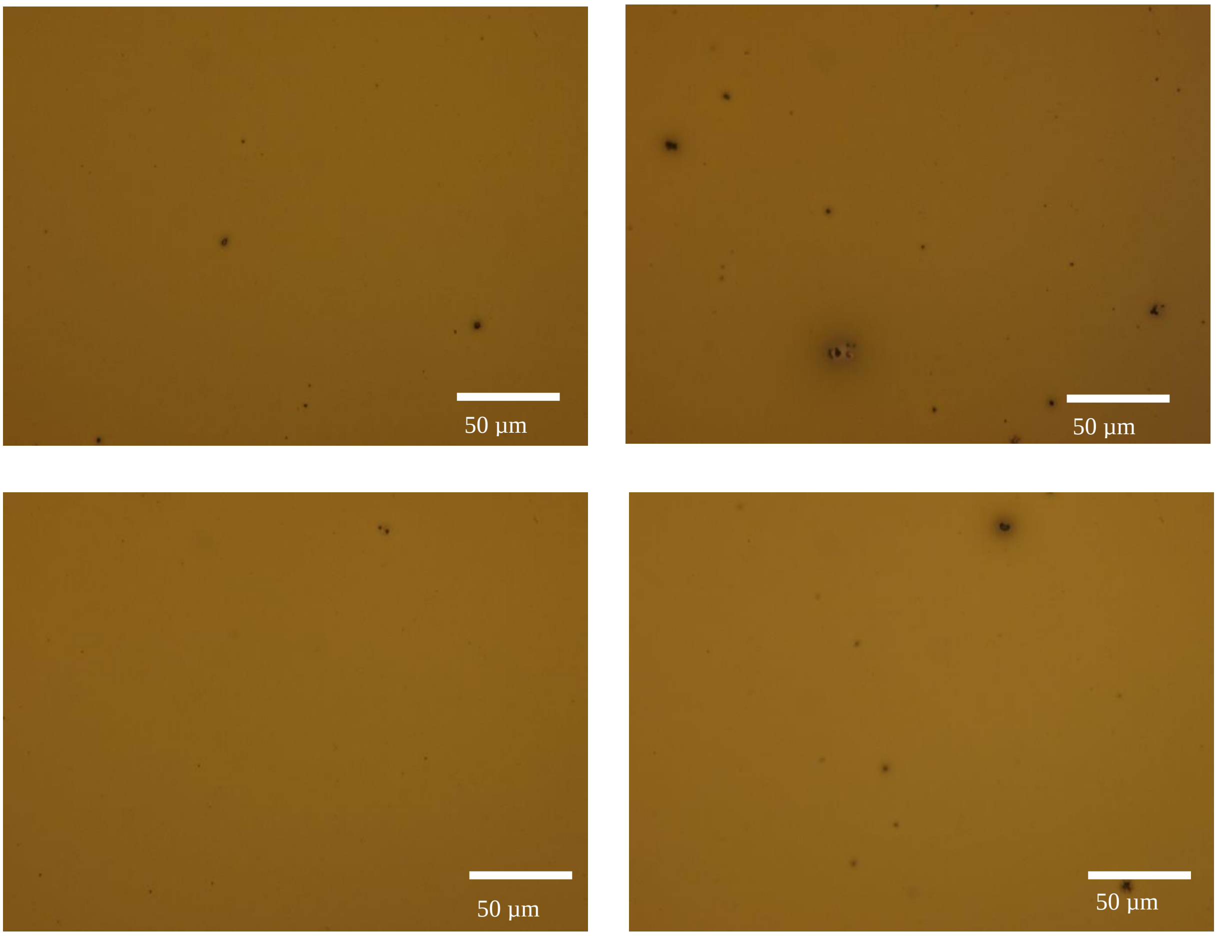

Figure 30. Images of the active layer recorded with light microscopy with a magnitude of 500x and a donor/acceptor ratio of 1/0.5. Upper row: no annealing treatment (left), annealing temp. of 120 °C (right). Lower row: annealing temp. of 160 °C (left), annealing temp. of 200 °C (right).

The pictures of the active layer consisting of half es much acceptor compared to the first approach show again quite homogeneous and smooth surfaces.

4.9.1. Comparison of solar cells containing different donor/acceptor ratios

The photovoltaic parameters PCE, FF, J_{sc} and V_{oc} of the solar cells containing a D/A ratio of 1/1 and 1/0.5 are summarized in Table 10. For reasons of simplicity, three different conditions were chosen (no annealing, annealing at 140 °C and 180 °C).

Table 10. Comparison of the photovoltaic parameters of the solar cells consisiting of D/A 1/1 and 1/0.5 at different annealing temperatures.

D/A ratio	**Temp. [°C]**	**V_{oc} [V]**	**J_{sc} [mA/cm^2]**	**FF [%]**	**PCE [%]**	**Thickness [nm]**
1/1	25	1.07 ± 0.04	-7.70 ± 0.52	33.4 ± 1.58	1.92 ± 0.22	55.7
1/0.5		1.01 ± 0.01	-5.09 ± 0.21	34.8 ± 0.73	1.25 ± 0.075	73.9
1/1	140	0.98 ± 0.03	-8.76 ± 0.56	39.8 ± 1.23	2.39 ± 0.30	55.7
1/0.5		1.05 ± 0.01	-6.84 ± 0.39	37.6 ± 0.71	1.88 ± 0.17	73.9
1/1	180	0.96 ± 0.02	-8.69 ± 0.44	39.3 ± 1.70	2.29 ± 0.29	55.7
1/0.5		1.01 ± 0.02	-7.94 ± 0.64	40.2 ± 2.01	2.24 ± 0.39	73.9

The average power conversion efficiency and short-circuit current is higher with higher amounts of acceptor in the blend solution for every annealing temperature. When the amount of acceptor is doubled, the current density is increasing by 34%, from -5.09 mA/cm^2 to 7.70 mA/cm^2, for the case without annealing. Besides, the PCE values are increased by 35%, from 1.25% towards 1.92%. Due to the fact, that the current density increases when charge transfer between donor and acceptor is facilitated[92], it is assumed that the charge transfer in more efficient in a D/A ratio of 1/1. Nevertheless, the slightly different layer thicknesses need to be considered, which leads to difficulties in comparison of the two composition variations.

Concerning V_{oc} and fill factors, there is no significant difference depending on the composition. However, in order to be capable of making meaningful statements and determining the optimum ratio of PCE-12/PMI-hT-PMI, further D/A ratio variations are necessary to investigate. For the purpose of further investigation towards D/A ratios, EQE spectra of the different compositions were recorded (see Figure 30).

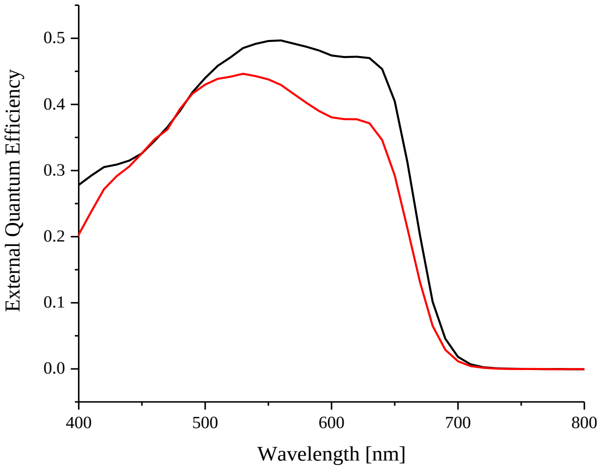

Figure 31. EQE spectra of the OSC devices consisting of D/A ratio 1/1 (black curve) and 1/0.5 (red curve).

The EQE of the device containing a D/A ratio of 1/1 was previously annealed at 120 °C, whereas the device of the D/A ratio of 1/0.5 was previously annealed at 180 °C.

The external quantum efficiency for the D/A ratio of 1/1 is 50%, whereas for the 1/0.5 ratio exhibits 45%. Since the EQE measurement determines the amount of current that a solar cell produces when exposed to photons of a certain wavelength, the results are in accordance to the higher short-circuit current values of the OSC devices with a higher amount of acceptor.

4.9.1.1. Light soaking experiment

The effect of light-soaking war investigated in a particular approach including illumination of the solar cells for 10 minutes. The photovoltaic parameters were measured before and after the experiment and are summarized in Table 11.

The results show a slightly increase in efficiency, resulting from light-soaking. The solar cell with a D/A ration exhibits 3% higher PCE values, whereas the solar cell with a D/A ratio of 1/0.5 exhibits an increase by 2.5%.

Table 11. Solar cell characteristics of two different composition variations (D/A of 1/1 and 1/0.5) before and after light soaking for 10 minutes.

Measurement	D/A ratio	V_{oc} [V]	J_{sc} [mA/cm^2]	FF [%]	PCE [%]
Before LS	1/1	1.08	-11.3	38.2	3.24
After LS	1/1	1.08	-11.5	38.4	3.35
Before LS	1/0.5	1.02	-8.76	38.7	2.39
After LS	1/0.5	1.04	-8.91	38.1	2.45

5. Experimental

5.1. Chemicals and Materials

Table 12. Chemicals used for syntheses and preparation of solar cells.

Chemicals	Purity Grade / Description	Supplier
Bromine, Br_2	> 99 %, iodometric	Merck
Iodine, I_2	99.99 % (trace metal basis), pellets	Sigma Aldrich
Perylene-3,4,9,10-tetracarboxylic dianhydride, PTCDA	>98.0%	TCI
2,6-diisopropylanilin, $H_2NC_6H_3(CH(CH_3)_2)_2$	97 %	Sigma Aldrich
Potassium fluoride, KF	99 %	Fluka
Tetrakis(triphenylphosphine)-Palladium, $Pd(PPh_3)_4$	99.9 %	abcr
Ethanol, EtOH	96 %	TU Graz
Aliquat 336	Highly viscous liquid	Sigma Aldrich
Toluol	99.5 %	TU Graz
Chlorobenzene, CB	99.8 %, anhydrous	Sigma Aldrich
Chloroform, CF	≥99.9 %	Sigma Aldrich
Dichloromethane, DCM	99.8 %	Fisher Scientific
Molybdenum(II)oxide	99.98 % (trace metal basis)	Sigma Aldrich
Silver, Ag	99.99 %, pellets	Kurt J. Lesker Company
PBDB-T/PCE-12	OS0804	One Material
Zinc acetate dehydrate	≥ 99.5 %	Fluka
2-Methoxyethanol	99.8 %, anhydrous	Sigma Aldrich
Ethanolamine	≥99 %	Sigma Aldrich
Methanol, MeOH	100 %	VWR

5.2. Synthesis

5.2.1. General information

Some of the syntheses were performed under inert N_2 conditions. Therefore, either a balloon was filled with nitrogen gas and the reaction mixtures were flushed, or the reactions were carried out by Schlenk line technique. Concerning the latter, the glassware was previously dried and heated with a heat gun to prevent oxygen and moisture exclusion. Nitrogen was flushed through the glassware three times, before loading it with reagents and solvent.

5.2.2. Analytical methods

5.2.2.1. Thin layer chromatography (TLC)

Reaction progresses were monitored by thin layer chromatography on silica gel plates (HP-TLC, aluminum sheets, Silica Gel 60 F_{254} purchased from Merck Millipore). All products and side-products were visible on the plates and the respective eluents are stated.

5.2.2.2. Column Chromatography

Column chromatography was performed for purification, using silica gel with particle size 0.04 nm – 0.063 mm, purchased from Macherey-Nagel upon elevated pressure. If not mentioned differently, the column was filled with the product-mixture by dry-loading.

5.2.2.3. Nuclear magnetic resonance (NMR) spectroscopy

The NMR spectra were recorded on a Bruker Advance III spectrometer device (300 MHz) with an auto sampler and on an Inova 500 (500 MHz; from Oxford Instruments). The measurements on latter were carried out by Petra Kaschnitz. Coupling constants (J) are described by absolute values in Hertz (Hz) and chemical shifts are listed in parts per million (ppm).

5.2.2.4. Mass spectrometry (MS)

The MALDI-TOF MS spectra were recorded on a ‘Micromass MALDI micro MX’ device from Waters and performed by Karin Bartl. The matrix constituted of *trans*-2-[3-(4-*tert*-butylphenyl)-2-methyl-2-propenylidene]malononitrile (DCTB) with a concentration of 10 mg/mL in tetrahydrofuran. The products were dissolved in methylene chloride in a concentration of 1 mg/mL and was mixed in a matrix/sample ratio of 7/2. The reference material constituted of polyethylene glycol (PEG) and the analysis of data was done with the MassLynx V4.1 software.

5.2.2.5. UV-Vis spectrometry

UV-Vis spectra were recorded on a spectrophotometer ‘UV-1800’ from Shimadzu. The measurements of the compounds were performed threefold in $CHCl_3$ as solvent. Therefore, a stock-solution of approx. 0.1 mg/mL was prepared three times and the solutions were adjusted in order to reach an absorbance below 1. The settings are summarized in Table 12.

Table 13. Settings used for the measurement of UV-Vis spectra in $CHCl_3$.

Start Wavelength [nm]	**800**
End Wavelength [nm]	350
Scan speed [nm/min.]	350
Slit Width [nm]	1.0
Data Interval	1

5.2.2.6. Fluorescence spectrometry

Three samples of the products dissolved in $CHCl_3$ were prepared initially, with an absorbance ≤ 0.1. In order to assure that, UV-Vis spectra were recorded on a spectrophotometer ‘Cary 50 Conc’ from Varian, before measuring fluorescence. The settings for the UV-Vis measurement are listed in Table 14.

Table 14. Settings for UV-Vis measurement.

Start Wavelength [nm]	**800**
End Wavelength [nm]	350
Scan speed [nm/min.]	70
Slit Width [nm]	1.0

Fluorescence was measured on a ‘FluoroLog 3’ spectrofluorometer from Horiba Scientific Jobin Yvon with an implemented ‘R2648’ photomultiplier from Hamamatsu. The used settings for this device are listed in Table 15. ‘Fluoreszenzorange’ was chosen as reference material purchased from Kremer Pigmente GmbH & Co. KG.

Table 15. Settings for fluorescence measurement.

Start Wavelength [nm]	**500**
End Wavelength [nm]	900
Scan speed [nm/min.]	70
Excitation Wavelength [nm]	490

5.2.2.7. Layer thickness and roughness

For this measurement, the contact profilometer ‘DekTakXT’ device from Bruker was used. Therefore, a scratch was performed with a blade onto the OSC devices, followed by the determination of the thickness and roughness on five different positions.

5.2.2.8. Light Microscopy

Pictures were taken of the active layer surfaces using a light microscope ‘BX60’, with a camera attached, both purchased from Olymp. The magnification used was 500 x.

5.2.2.9. External Quantum Efficiency

The EQE spectra were recorded for each mass ratio (D/A 1/1 and 1/0.5) once. Therefore, the best cell of each approach was measured. The IPCE (incident-photon-to-current) measuring system comprised of a MuLTImode 4-AT monochromator device from Amko, a xenon lamp ‘LPS 210-U’ from Amko and a Keithley 2400 SourceMeter. The OSC devices were transferred to a custom-made measuring box sealed under nitrogen. The actual measurement was carried out outside the glove-box, with an initial calibration step using a photodiode (1.2 mm^2). The EQE spectra were recorded in the range of 350-900 nm.

5.2.3. Synthesis of 2-(2,6-diisopropylphenyl)-1H-benzo[10,5]anthra[2,1,9-def]isoquinoline-1,3(2H)-dione – compound 1

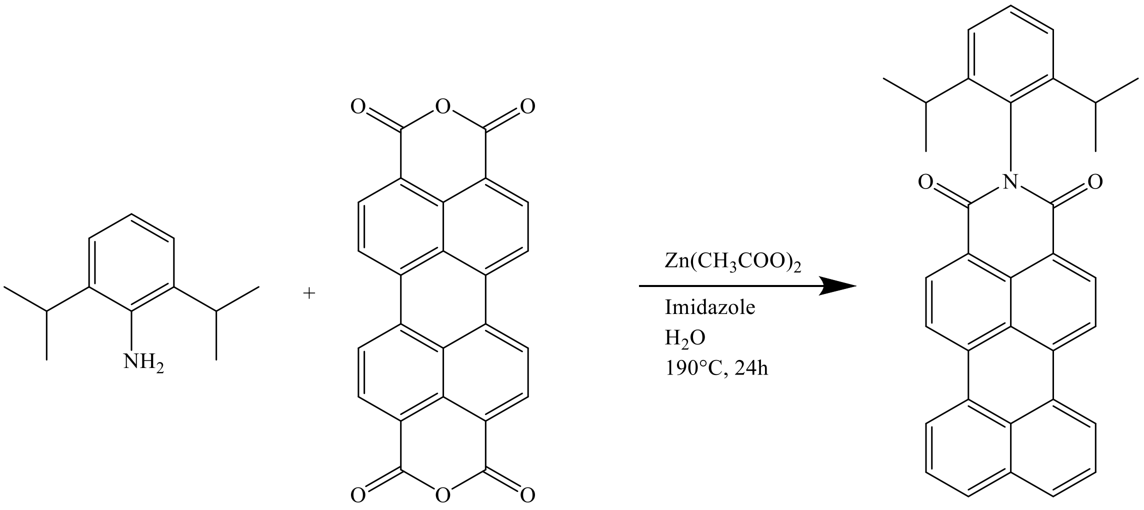

1

A mixture of perylene-3,4,9,19-tetracarboxylic dianhydride (PTCDA) (25 g, 63.7 mmol), zinc acetate (9.40 g, 42.8 mmol), 2,6-Diisopropylaniline (6.34 mL, 33.6 mmol), imidazole (127.5 g) and dest. water (30 mL) was stirred for 24 h and 190°C in an autoclave. Afterwards, the mixture was cooled down to room temperature and furthermore stirred for 66 h. After stirring, it was rinsed with water (180 mL) and acidified to a pH of 2 with hydrochloric acid followed by filtration through a vacuum frit. The filter cake was extracted in a Soxhlet extractor with $CHCl_3$ as solvent for 48 h. Purification gave the red product PMI (**1**) in a 23% yield and purification was carried out by column chromatography with $CHCl_3$ as eluent.

$C_{34}H_{27}NO_2$ = 481.6 g/mol

^{1}H-NMR (300 MHz; $CDCl_3$): δ = 8.66 (d, 2H, 8.2), 8.53 – 8.41 (m, 4H), 7.92 (d, 2H, *J* = 8.26 Hz), 7.71 – 7.60 (m, 2H), 7.52 – 7.44 (m, 1H), 7.32 (d, 2H, *J* = 7.50), 2.85 – 2.69 (septet, 2H, *J* = 13.45 Hz), 1.19 (d, 12H, *J* = 6.88 Hz) ppm.

5.2.4. Synthesis of 8,8'-(thiophene-2,5-diyl)bis(2-(2,6-diisopropylphenyl)-1H-benzo[10,5]anthra[2,1,9-def]isoquinoline-1,3(2H)-dione) – compound 6

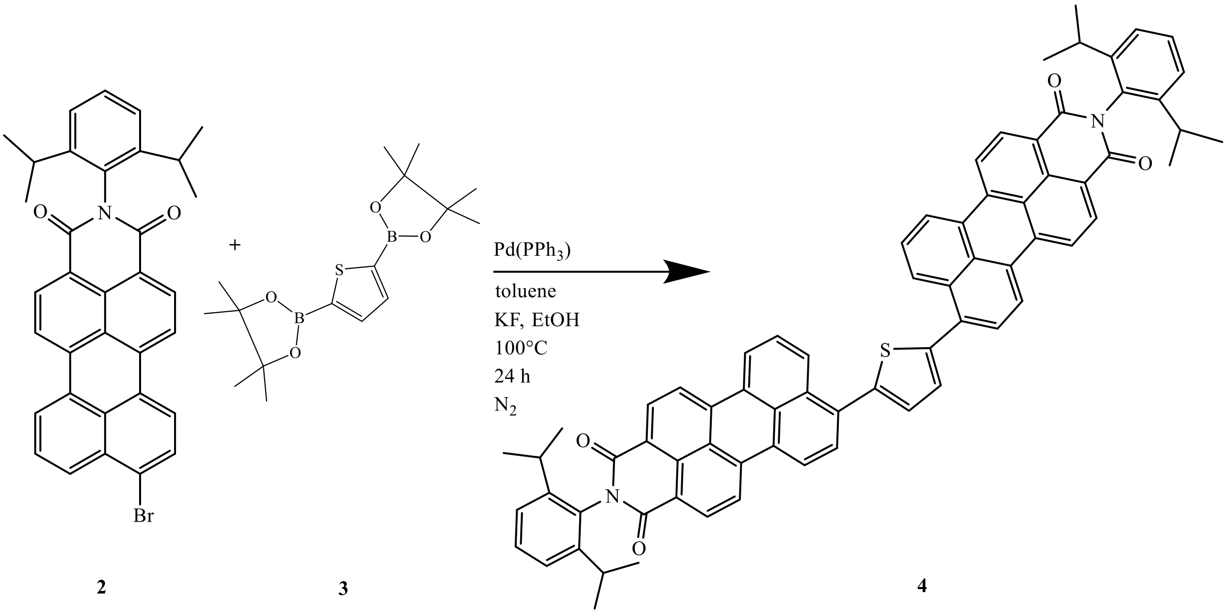

PMI-Br (**2**) (111 mg, 0.20 mmol, 1.1 equiv.) was suspended in 12 mL toluene in a two- necked flask under inert conditions. Afterwards, thiophene-2,5-diboronic acid bis(pinacol)ester (**3**) (30 mg, 0.089 mmol, 0.5 equiv.), Pd(PPh$_3$)$_4$ (10 mg, 5 mol%), aqueous potassium fluoride solution (2 mL), ethanol (0.2 mL) and one drop Aliquat 336 were added and heated to reflux for 24 h. The mixture was then cooled to room temperature and washed with saturated brine and water in a separation funnel. The organic layer was dried over Na_2SO_4 and filtered. After solvent evaporation under reduced pressure, the residue was purified by silica-gel chromatography with toluene/acetone (99:1) as eluent, using a gradient towards a ratio of 99:5. A violet solid of PMI-thio-PMI (**4**) was obtained in a 30-40% yield.

^{1}H-NMR (300 MHz; $CDCl_3$): δ = 8.71 (d, 4H, *J* = 7.71 Hz), 8.62 – 8.46 (m, 9H), 7.88 (d, 1.5H, *J* = 7.50 Hz), 7.76 (t, 2H, *J* = 16.1 Hz), 7.54 – 7.45 (m, 3.5H), 7.39 – 7.29 (m, 18H), 2.86 – 2.70 (septet, 4H), 1.20 (d, 24H, *J* = 6.8 Hz) ppm.

MS (MALDI TOF): $[M]^+$ = 1042.3925 (measured), 1043.29 (calculated for $C_{72}H_{54}N_2O_4S$)

5.2.5. Synthesis of 8,8'-(3-hexylthiophene-2,5-diyl)bis(2-(2,6-diisopropylphenyl)-1H-benzo[10,5]anthra[2,1,9-def]isoquinoline-1,3(2H)-dione) (compound 7)

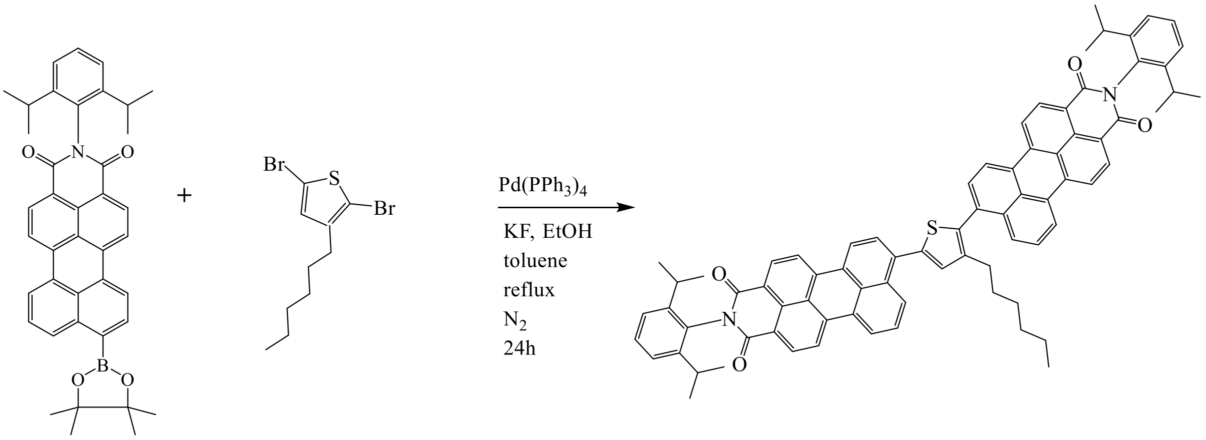

5 **6** **7**

Compound **5**, provided by Matīss Reinfelds, (111 mg, 0.20 mmol, 1.1 equiv.) was suspended in 12 mL toluene in a two- necked flask under inert conditions. Afterwards, compound 5 (30 mg, 0.089 mmol, 0.5 equiv.), Pd(PPh$_3$)$_4$ (10 mg, 5 mol%), aqueous potassium fluoride solution (2 mL), ethanol (0.2 mL) and one drop Aliquat 336 were added and heated to reflux for 24 h. The mixture was then cooled to room temperature and washed with saturated brine and water in a separation funnel. The organic layer was dried over Na$_2$SO$_4$ and filtered. After solvent evaporation under reduced pressure, the residue was purified by silica-gel chromatography with methylene chloride/cyclohexane as eluent, using a gradient. A purple solid of PMI-hT-PMI (**7**) was obtained in a 30-40% yield.

^{1}H-NMR (300 MHz; CDCl$_3$): δ = 8.71 – 8.65 (m, 4H), 8.58 (d, 1H, *J* = 8.49), 8.56 – 8.44 (m, 8H), 8.09 (d, 1H, *J* = 8.45 Hz), 7.85 (d, 1H, *J* = 7.86 Hz), 7.79 (d, 1H, *J* = 7.60 Hz), 7.77 – 7.68 (m, 2H), 7.40 – 7.32 (m, 5H), 2.85 – 2.74 (septet, 4H, *J* = 13.2 Hz), 2.60 – 2.51 (m, 2H), 1.68 – 1.60 (m, 2H), 1.30 – 1.13 (m, 6H), 1.20 (d, 24H, *J* = 6.80 Hz), 0.82 – 0.77 (m, 3H) ppm.

MS (MALDI TOF): $[M]^+$ = 1126.4100 (measured), 1127.46 (calculated for $C_{78}H_{66}N_2O_4S$)

Synthesis of 8,8',8'',8'''-(ethene-1,1,2,2-tetrayltetrakis(benzene-4,1-diyl))tetrakis(2-(2,6-diisopropylphenyl)-1H-benzo[10,5]anthra[2,1,9-def]isoquinoline-1,3(2H)-dione)

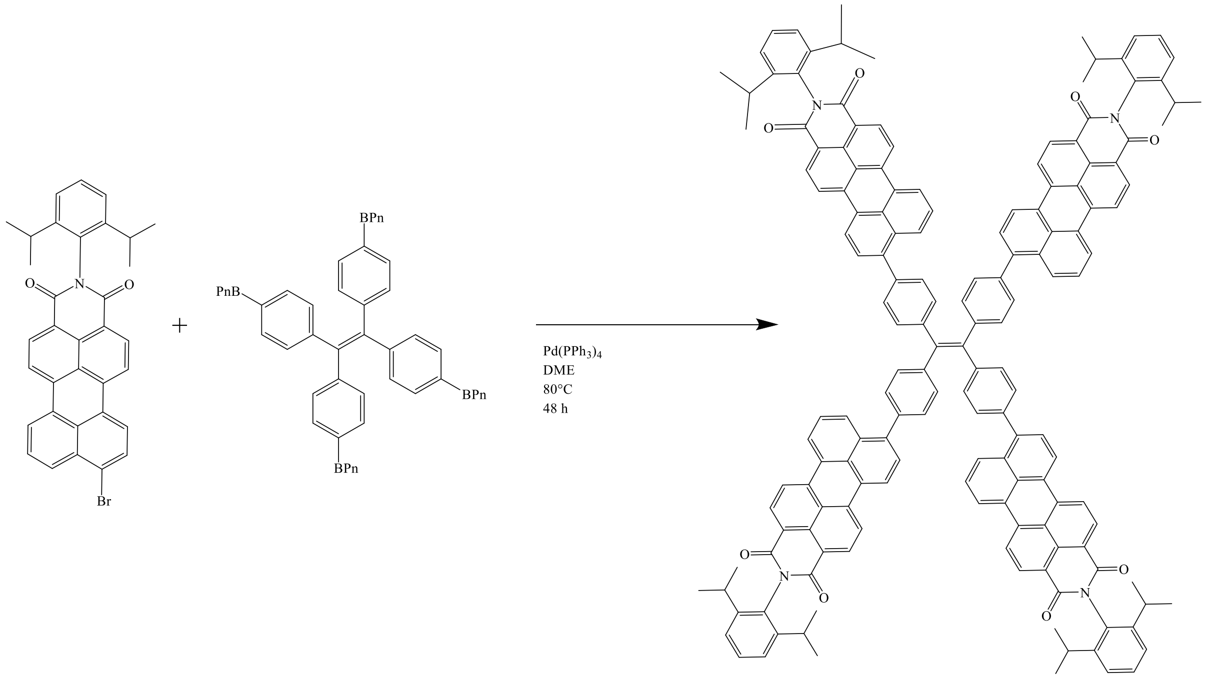

2 **7** **8**

PMI-Br (**2**) (1000 mg, 1.78 mmol, 8.8 equiv.) was suspended in 120 mL DME in a three-necked round flask. Tetraphenylethylene-boronic acid pinacol ester, provided by Rene Nauschnig, (169 mg, 0.202 mmol, 1 equiv.), aqueous potassium fluoride solution (16 mL), ethanol (1.6 mL) and one drop of aliquat were added. The mixture was flushed with N_2 gas for 20 minutes, before and after the addition of $Pd(PPh_3)_4$ (25.8 mg, 5 mol%). The reaction mixture was stirred and heated at 80°C to reflux for 48 h. After cooling to room temperature, the solvent was removed by rotary evaporation. The mixture of solids was diluted in toluene and washed with brine in a separation funnel. The organic layer was dried over Na_2SO_4 overnight.

5.3 Organic solar cells

5.3.1. General procedure

The organic solar cells were assembled in an inverted structure, consisting of the top and bottom electrodes (Ag and ITO), hole and electron transport layer (MoO_3 and ZnO) and the photoactive layer, including donor and acceptor. The procedure of the assembly is described in the following chapters.

5.3.1.1. Substrate preparation

Glass substrates coated with indium tin oxide (ITO, 15 x 15 x 1.1 mm), purchased from Luminescence TehcnologyCorporation, exhibiting a sheet resistance of 15 Ω. The substrates were initially cleaned with acetone, followed by an ultrasonic bath in 2-propanol at 40 °C with a duration of 30 minutes. After the ultrasonic treatment, the substrates were dried with compressed air and the surface was activated via plasma-etching. This was carried out with in the 'Femto' etcher device from Diener Electronics, with a constant oxygen flow for three minutes. Afterwards, the substrates were transferred into a nitrogen filled glove-box 'LabMaster dp' from MBraun.

5.3.1.2. ZnO interfacial layer

The ZnO layer was deposited via a sol-gel procedure. Therefore, 500 mg zinc acetate dihydrate was mixed with 5 mL 2-methoxyethanol and 150 µL ethanolamine. This precursor was mixed under ambient conditions for 18 h, followed by the transfer into the glove-box for further stirring. The previously prepared ITO-substrates were spin-coated with 35 µL of ZnO-precursor using a speed of 4000 rpm with an acceleration of 2000 rpm/s for 30 s, in order to obtain a layer thickness of 20 – 30 nm. The spin-coater device was the model 'WS-650MZ-23NPPB' purchased from Laurell Technologies. The annealing treatment was carried out under ambient conditions at 150 °C for 10 min.

5.3.1.3. Active Layer deposition

The acceptor material was dissolved in chlorobenzene and stirred for at least 1 h at 50 °C, followed by the addition of the donor materials PCE-12 and further stirring overnight at 50 °C. The concentration of the acceptor was 10 mg/mL (D/A ratio of 1/1) for the first approach, and 5 mg/mL for the second (D/A of 1/0.5). The spin-coating speed was 2000 rpm (ratio 1/1) and 1500 rpm (ratio 1/0.5), respectively. The actual spin-coating of the D/A blend was done for 1 min., followed by a drying step with 4000 rpm and 4000 rpm/s acceleration for 5 seconds for each approach. Afterwards, the substrates were annealed at different temperatures for 10 minutes.

5.3.1.4. MoO_3 interfacial layer and Ag deposition

The hole-transport layer of MoO_3 and the top Ag electrodes were thermally evaporated with a thickness of 10 nm and 100 nm, respectively. A shadow-mask was utilized in order to obtain an active electrode area of 0.09 cm^2. The thermal evaporation was carried out in vacuo with minimum 1 x 10^{-5} bar.

5.3.2. Characterization of BHJ OSC devices

5.3.2.1. I-V Characteristics

The settings for the determination of the IV curves under illumination and dark conditions are summarized in Table 16. The measurement was carried out with a Keithley 2400 SourceMeter device using a costum-made LabView software. The light source originated from a Dedolight DEB400D lamp, with an intensity of 100 mW/cm^2, mimicking a spectrum as AM 1.5G. If not mentioned otherwise, the active area was enclosed with a shadow-mask to an active area of 0.070225 cm^2. The photovoltaic parameters PCE, FF, V_{oc} and J_{sc} were determined, and if not mentioned otherwise, the average of 8 best cells was calculated.

Table 16. Settings of the I-V measurement of the OSC devices.

Start [mV]	**1500**
End [mV]	-500
Compliance [mA]	100
Number of Points	100
Overwrite max. compliance [mA]	500
Delay [ms]	100
Step width [V]	-0.02

5.3.2.2. UV-Vis measurement of the films

The absorption spectra of thin films of donor, acceptor and D/A blends were measured on glass substrates. The materials were diluted in $CHCl_3$ and spin-coated onto the substrates with a concentration of 10 mg/mL. The coating procedure was carried out under inert conditions in N_2 filled a glove-box. The settings are summarized in Table 17, and the measurement was done with a ‘Lambda 35’ UV-Vis spectrometer from Perkin Elmer.

Table 17. Settings used for the UV-Vis measurement of the thin films.

Start Wavelength [nm]	**800**
End Wavelength [nm]	400
Scan speed [nm/min.]	240
Slit Width [nm]	1.0
Data Interval [nm]	1

5.3.2.3. Layer thickness and roughness

For this measurement, the contact profilometer ‘DekTakXT’ device from Bruker was used. Therefore, a scratch was performed with a blade onto the OSC devices, followed by the determination of the thickness and roughness on five different positions.

5.3.2.4. Light Microscopy

Pictures were taken of the active layer surfaces using a light microscope ‘BX60’, with a camera attached, both purchased from Olymp. The magnification used was 500 x.

5.3.2.5. External Quantum Efficiency

The EQE spectra were recorded for each mass ratio (D/A 1/1 and 1/0.5) once. Therefore, the best cell of each approach was measured. The IPCE (incident-photon-to-current) measuring system comprised of a MuLTImode 4-AT monochromator device from Amko, a xenon lamp ‘LPS 210-U’ from Amko and a Keithley 2400 SourceMeter. The OSC devices were transferred to a custom-made measuring box sealed under nitrogen. The actual measurement was carried out outside the glove-box, with an initial calibration step using a photodiode (1.2 mm^2). The EQE spectra were recorded in the range of 350-900 nm.

6. Summary and Conclusion

Two acceptor materials consisting of thiophene-coupled perylene monoimide units (PMI-thio-PMI, PMI-hT-PMI) were successfully synthesized via Suzuki-coupling in yields of 30-40% and characterized by ^{1}H-NMR spectroscopy, mass spectrometry, UV-Vis absorption and emission spectroscopy. The Suzuki-coupling reaction, providing the basis of the synthesis of PMI-thio-PMI and PMI-hT-PMI, was investigated towards additives, temperature, reaction time and type of base. The purpose of the optimization of Suzuki-coupling was to find conditions which prevent the formation of side-products during the reaction. The results show that the addition of ethanol is beneficial for an efficient conversion towards the products. Moreover, different bases were tested, in which potassium fluoride showed advantageous effects on the cross-coupling, being the best choice. Besides, it was found that replacing toluene as solvent by dimethoxyethane (DME) leads to diminished recrystallization steps as purification procedure.

Since more coupling positions signify more possible side-products, the synthesis of the quadrupole-linked $(PMI)_4TPE$ compound needs further optimization in terms of reaction conditions and starting materials. Therefore, leaving groups could be varied, employing for example iodine instead of bromide, or the choice of a more efficient Pd-catalyst would presumably have beneficial effects on the conversion towards the desired product.

Optical spectroscopy of PMI-thio-PMI and PMI-hT-PMI revealed absorption ranges between 450 nm and 600 nm, showing an absorption maximum at 531 nm and 536 nm, respectively. In this regard, band gaps were determined optically using the absorption spectra. The determination of the band gap revealed a value of 2.06 eV for PMI-thio-PMI and 2.11 eV for the hexylthiophene-based compound. These values differ by 0.32 eV and 0.36 eV, respectively, comparted to the results, determined by DFT-calculations. By using the fluorescence spectra, the relative quantum yield of 47.2% for PMI-thio-PMI and 55.0% for PMI-hT-PMI, respectively.

PMI-hT-PMI, including the hexylthiophene-linker, is fulfilling the requirements for the application in OSCs, like good solubility, appropriate absorption properties and suitable HOMO/LUMO energy levels (determined by DFT calculations) referred to the donor material PCE-12. However, this was not the case for PMI-thio-PMI, which exhibits tremendous solubility issues.

Bulk heterojunction organic solar cells were fabricated in an inverted structure using PBDB-T as donor material with ZnO and MoO_3 as interfacial layers, ITO and Ag as electrodes. The solar cells were characterized by I-V measurements, light microscopy, external quantum efficiencies and UV-Vis spectroscopy, measured on thin films.

The devices were investigated towards donor/acceptor ratio, annealing temperature, light-soaking and stability. The tested D/A ratio were 1/1 and 1/0.5. In general, the solar cells with the higher amount of acceptor (ratio 1/1) achieved better results concerning power conversion efficiency, fill factor, J_{sc} and V_{oc}. In order to achieve higher efficiencies, the effect of annealing was examined. The temperatures ranged from 80 °C up to 200 °C, leading to an optimum annealing temperature of 120 °C for the D/A ratio of 1/1 and 180 °C for the ratio 1/0.5 The solar cell consisting of the higher amount of acceptor reached the highest efficiency of 3.35%, after annealing at 120 °C and light-soaking for 10 minutes, with high open-circuit voltages above 1 V. In the case of half as much acceptor, the best solar cell achieved an efficiency of 3.31%, also exhibiting a V_{oc} of >1 V. Since the average photovoltaic parameters of the OSCs with a D/A ratio of 1/1 outgo the performance of the cells consisting of D/A ratio of 1/0.5, further experiments were performed with the devices having higher amounts of acceptor.

Interestingly, it was found out, that the performance of the solar cells during storage under inter conditions was drastically improved. The efficiency measured directly after fabrication of one certain cell was 2.75%, whereas after 168 hours of storage, without exclusion of light, the efficiency reached 3.90%. When it comes to short-circuit current, an increase by 50% was observable, while the FF and V_{oc} did not change. Nevertheless, to make a valid statement, average values of many additional devices would need to be compared.

The maximum power point tracking approach revealed high stability related to the OSCs comprising PMI-hT-PMI as acceptor material. After 66 hours of illumination by a LED lamp, the performance showed an overall improvement, reaching an efficiency of 4.25% afterwards, compared to the starting value of 3.90%.

According to the findings of this work, hexylthiophene-coupled perylene monoimides represent a very promising acceptor material for the purpose of non-fullerene based organic solar photovoltaics.

7. References

(1) www.nationalgeographic.com/science/space/solar-system/the-sun

(2) E. Becquerel, C. R. Acad. Sci., 9, 1839, 145.

(3) W. Smith, Nature, 1873, 303.

(4) Cleveland, J.C.; Morris, C. G., Dictionary of Energy, Elsevier, 2014, p. 8.

(5) Fritts, C.E., Proc. Am. Assoc. Adv. Sci., 33, 1883, p. 97.

(6) The Nobel Prize in Physics 1921, NobelPrize.org.

(7) Millikan, R., Physical. Review, 1916, 7.

(8) Einstein, A., Annalen der Physik, 1905, 17, 132-148.

(9) The Nobel Prize in Physics 1923, NobelPrize.org.

(10) pbs.org/transistor/science/events/pnjunc.html

(11) Cleveland, J.C.; Morris, C. G.; Handbook of Energy: Chronologies, Top Ten Lists, and Word Clouds, Elsevier, 2013, p. 292.

(12) D. Chapin, C. Fuller, and G. Pearson, J. Appl. Phys., 1954, 25, 676.

(13) National Renewable Energy Laboratory, 2019.

(14) Tao, M., Electrochemical Society Interface, 2008, 17, 30-35.

(15) Dimroth, F., IEEE Journal of Photovoltaics, 2016, 6, 343-349.

(16) Tang, Y.; Huiliang, S.; Ziang, W.; Yujie, Z.; Guangye, Z.; Mengyao, S.; Xin, Z.; Xia, W.; Weipeng, S.; Xianghe, Z.; Bin, L.; Wei, C.; Qiaogan, L.; Han, Y.; Xugang, W., Adv. Sci, 6, 2019, 1901773.

(17) Brabec, C. J.; Sariciftci, N. S.; Hummelen, J.C., Adv. Funct. Mater., 2001, 11, 15-25.

(18) Kerp, H. R.; Donker, H.; Koehorst, R. B. M; Schaafsma, T. J.; van Fassen, E. E., Chem. Phys. Lett., 298, 1998, 302-308.

(19) Hoppe, H.; Sariciftci, N. S., J. Mater. Res., 2004, 19, 1924-1945.

(20) Dimitrakopoulos, C. D.; Mascaro, D. J., IBM J. Res. Dev., 2001, 45,11-27.

(21) Gregg, B. A.; Hanna, M. C., J. Appl. Phys. 93, 2003, 3605-3614.

(22) Abdulrazzaq, O. A.; Viney, S.; Shawn, B.; Enkeleda, D.; Alexandru, S.B., Particul. Sci. Technol., 2013, 31, 427-442.

(23) Lingxian M.; Yamin, Z.; Xiangjian, W.; Chenxi, L.; Xin, Z.; Yanbo, W.; Xin, K.; Zuo, X.; Liming, D.; Ruoxi, X.; Hin-Lap, Y; Yong, C.;Yongsheng, C., Science, 361, 2018, 1094-1098.

(24) Hoppe, H.; Sariciftci, N.S., J. Mater. Res., 2004, 19, 1928-1929.

(25) Luceno-Sanchez, J.A; Diez-Pascual, A.M.; Capilla, R.P., Int. J. Mol. Sci., 2019, 20, 976.

(26) Gregg, B.A., J. Phys. Chem. B., 2003, 107, 4688-4698.

(27) Scharber, M.; Mühlbacher, D.; Koppe, M.; Denk, P.; Waldauf, C.; Heeger, A. J.; Brabec, C. J., Adv. Mater., 2006, 18, 789–794.

(28) Hashimoto, Y.; Hamagaki, M., Electr. Eng. Jpn., 2006, 154, 379–384.

(29) Ayzner, A. L.; Tassone, C. J.; Tolbert, S. H.; Schwartz, B. J., J. Phys. Chem., 2009, 113, 20050-20060.

(30) Saunder, B. R.; Turner, M. L., Adv. Colloid. Interfac. Science, 2008, 138, 1-23.

(31) Wang, G.; Jiu, T.; Tang, G.; Li, J.; Li, P.; Song, X.; Lu, F.; Fang, J. ACS Sustain. Chem. Eng. 2014, 2, 1331-1337.

(32) Liao, S. H.; Jhuo, H. J.; Yeh, P. N.; Cheng, Y. S.; Li, Y. L.; Lee, Y. H.; Sharma, S.;Chen, S. A. Sci. Rep. 2014, 4, 4–10.

(33) Chang, H.; Chen, Z.; Yang, X.; Yin, Q.; Zhang, J.; Ying, L.; Jiang, X. F.; Xu, B.; Huang, F.; Cao, Y. Org. Electron. physics, Mater. Appl. 2017, 45, 227–233.
(34) Hou, W.; Xiao, Y.; Han, G.; Lin, J. Y. Polymers, 2019, 11, 1–46.
(35) Fraga Domínguez, I.; Distler, A.; Lüer, L., Adv. Energy Mater. 2017, 7, 161320.
(36) Ans M.; Ayub K.; Muhammad S.; Iqbal J., Comput. Theor. Chem, 2019, 1161, 26-38.
(37) Patil, Y.; Misra, R.., Chem. Rec. 2018, 18, 1350–1364.
(38) Kozma E.; Catellani M., Dyes and Pigments, 2013, 98, 160-179.
(39) Hu, Y.; Chen, S.; Zhang, L.; Zhang, Y.; Yuan, Z.; Zhao, X.; Chen, Y. J. Org. Chem. 2017, 82, 5926-5931.
(40) Brabec, C. J.; Shaheen, S. E.; Winder, C.; Sariciftci, N. S.; Denk, P., Appl. Phys. Lett., 2002, 80, 1288-1290.
(41) Steim, R.; Kogler, F. R.; Brabec, C. J. J. Mater. Chem. 2010, 20, 2499–2512.
(42) Kardos M. D.R.P. 276956, Friedlanders Fortschr. Teerfarbenfabr.1917, 1492.
(43) Choi M.J. Forensic Sci. Int., 2007, 173, 154-160.
(44) Zhao Y.; Zhang X.; Li D.; Liu D.; Jiang W.; Han C. Luminescence, 2009, 24, 140-143.
(45) Ego C. et al. J. Am. Chem. Soc., 2003, 125, 437-443.
(46) Oregan B.; Gratzel M.; Nature, 1991, 353, 737–740.
(47) Schmidt-Mende L.; Fechtenkötter, A.; Müllen, K.; Moons, E.; Friend, R. H.; MacKenzie, J. D., Science, 2001, 293, 1119-1122.
(48) Li J. L.; Dierschke F.; Wu J.S.; Grimsdale A.C.; Müllen K., J. Mater. Chem. 2006, 16, 96–100.
(49) Li C.; Wonneberger H., Adv. Mater., 2012, 24, 613-636.
(50) Zhan X.; Tan, Z.; Domercy, B.; An, Z.; Zhang, X.; Barlow, S.; Li, Y.; Zhu, D.; Kippelen, B.; Marder, S. R., J. Am. Chem. Soc., 2007, 129, 7246-7247.
(51) Sharma G. D.; Suresh P.; Mikroyannidis J. A.; Stylianakis M. M., J. Mater. Chem., 2010, 20, 561-567.
(52) Zhou, E.; Cong, J.; Wei, Q.; Tajima, K.; Yang, C.; Hashimoto, K., Angew. Chem. Int. Edt., 2011, 50, 2799-2803.
(53) Chen W.; Xuan, Y.; Guankui, L.; Xiangjian, W.; Yongsheng, C.; Qichun, Z., J. Mater. Chem. C., 2015, 3, 4698-4705.
(54) Jingbo, Z.; Yunke, L.; Haoran, L.; Yuhang, L.; Kui, J.; Cheng, M.; Tingxuan, M.; Joshua, Y. L., L.; Huawei, H.; Demei, Y.; He, Y., Energy Environ. Sci., 2015, 8, 520.
(55) Liu, J.; Chen, S.; Qian, D.; Gautam, B.; Yang, G.; Zhao, J.; Bergqvist, J.; Zhang, F.; Ma, W.; Ade, H.; Inganäs, O.; Gundogdu, K.; Gao, F.; Yan, H., Nat. Energy, 2016, 1, 16089.
(56) Cremer J.; Bäuerle P., J. Mater. Chem., 2006, 16, 874-884.
(57) Cremer J.; Mena-Osteritz E. M.; Pschierer N. G.; Müllen K.; Bäuerle P., Org. Biomol. Chem., 2005, 3, 985-995.
(58) Cremer J.; Bäuerle P., Eur. J. Org. Chem., 2005, 17, 3715–3723.
(59) Zhang, Y.; Xiao, Y.; Xie, Y.; Zhu, L.; Shi, D.; Chen, C., Org. Electron., 2015, 21, 184-191.
(60) Tomizaki, K.; Loewe, R. S.; Kirmaier, C.; Schwartz, J. K.; Retsek, J. L.; Bocian, D. F.; Holten, D.; Lindsey, J. S., J. Org. Chem., 2002, 67, 6519-6534.
(61) Qin, R.; Guo, D.; Li, M.; Li, G.; Bo, Z.; Wu, J., Appl. Energy Mater., 2019, 2, 305-311.

(62) Cui Y.; Yao, H.; Zhang, J.; Zhang, T.; Wang, Y.; Hong, L.; Xian, K.; Zhang, S.; Peng, J.; Wei, Z.; Gao, F.; Hou, J., Nat. Commun., 2019, 10, 2515.

(63) Tamao, K.; Sumitani, K.; Kumada, M. J. Am. Chem. Soc. 1972, 94, 4374.

(64) Neumann, S. M.; Kochi, J. K. J. Org. Chem. 1975, 40, 599-606.

(65) Yamamura, M.; Moritani, I.; Murahashi, S. J. Organomet. Chem. 1975, 91, 39-42.

(66) Milstein, D.; Stille, J. K. J. Am. Chem. Soc. 1979, 101, 4992-4998.

(67) Miyaura, N.; Yamada, K.; Suzuki, A., Tetrahedron Lett. 1979, 36, 3437–3440.

(68) The Nobel Prize in Chemistry 2010, NobelPrize.org

(69) Aliprantis, A. O.; Canary, J. W.; J. Am. Chem. Soc. 1994, 116, 6985-6986.

(70) Adamo C.; Amatore C.; Ciofini I.; Jutand A.; Lakmini H., J. Am. Chem. Soc., 2006, 128, 6829-6836.

(71) Littke, A. F.; Dai, C.; Fu, G. C., *J. Am. Chem. Soc.* 2000, 122, 4020–4028.

(72) Gaussian 09, Revision D.01, Frisch, M. J.; Trucks, G. W.; Schlegel, H.B.; Scuseria, G. E.; Robb, M. A.; Cheeseman, J. R.; SCalmani, V.; Barone, V.; Mennucci, B.; Petersson, G. A.; Nakatsuji, H.; Caricato, M.; Li, X.; Hratchian, H. P.; Izmaylov, A. F.; Bloino, J.; Zheng, G.; Sonnenberg, J. L.; Hada, M.; Ehara, M.; Toyota, K.; Fukada, R.; Hasegawa, M.; Ishida, M.; Nakajima, T.; Honda, Y.; Kitao, O.; Nakai, H.; Vreven, T.; Montgomery J.A.; J. E. Peralta, F. Ogliaro, M. Bearpark, J. J. Heyd, E. Brothers, K. N. Kudin, V. N. Staroverov, T. Keith, R. Kobayashi, J. Normand, K. Raghavachari, A. Rendell, J. C. Burant, S. S. Iyengar, J. Tomasi, M. Cossi, N. Rega, J. M. Millam, M. Klene, J. E. Knox, J. B. Cross, V. Bakken, C. Adamo, J. Jaramillo, R. Gomperts, R. E. Stratmann,, O. Yazyev, A. J. Austin, R. Cammi, C. Pomelli, J. W. Ochterski, R. L. Martin, K. Morokuma, V. G. Zakrzewski, G. A. Voth, P. Salvador, J. J. Dannenberg, S. Dapprich, A. D. Daniels, O. Farkas, J. B. Foresman, J. V. Ortiz, J. Cioslowski, D. J. Fox, Gaussian, Inc., Wallingford CT, 2013.

(73) Feiler L.; Langhals H.; Polborn K., Liebigs. Ann., 1995, 1229-1244.

(74) Huimin W.; Nan J.; Nan Z.; Ying Z.; Baoxiang G., Chin. J. Chem., 2014, 32, 356-360.

(75) Kothandaraman G.; Rajaram J.; Kuriacose J. C., Proceedings of the Indian Academy of Sciences – Section A, 1970, 72, 144-148.

(76) Leifang L.; Yuhong Z.; Bingwei X., J. Org. Chem., 2006, 71, 3994-3997.

(77) Shenghai L.; Yingjie L.; Jungang C.; Suobo Z., J. Org. Chem., 2007, 72, 4067-4072.

(78) Miyaura N., J. Org. Chem., 2002, 654, 54-57.

(79) Xiaoyin Y.; Xi D.; Müllen K., Chem. Asian. J., 2008, 3, 759-766.

(80) Lima C. F. R. A. C.; Rodrigues A. S. M. C.; Silva V. M. L.; Silva A. M. S.; Santos L. M. N. B. F.; Chem. Cat. Chem., 2014, 6, 1291-1302.

(81) Sinclair, D. J.; Sherburn, M.S., J. Org. Chem., 2005, 70, 3730-3733.

(82) Fluoreszenzorange, www.kremer-pigmente.com/media/pdf/94738.pdf

(83) Lu, Q.; Qiu, M.; Zhao, M.; Li, Y., Polymers, 2019, 11, 958.

(84) Hori, T.; Moritou, H.; Fukuoka, N.; Sakamoto, J.; Fujii, A.; Ozaki, M., Materials, 2010, 3, 4915-4921.

(85) Benanti, T. L.; Venkataraman, D., Photosynth. Res., 2006, 87, 73-81.

(86) Chen, Y.; Liu, T.; Hu, H.; Ma, T.; Lin Lai, J. Y.; Zhang, J.; Ade, H.; Yan, H., Adv. Energ. Mater., 2018, 8, 1801203.

(87) Yang, X.; Uddin, A., Renew. Sust. Energ. Rev., 2014, 30, 324-226.

(88) Ourahmoun, O., J. Nano-Electron. Phys., 2019, 11, 02004.

(89) Mateker W. R.; McGehee, M. D., Adv. Mater., 2017, 29, 1603940.

(90) Lee, P. H.; Torng, C. C.; Li, Y. C., Appl. Math. Model., 2011, 35, 4023-4030.

(91) Peters, C. H.; Sachs-Quintana, I. T.; Mateker, W. R.; Heumueller, T.; Rivnay, J.; Noriega, R., Beiley, Z. M.; Hoke, E. T.; Salleo, A.; McGehee, M. D., Adv. Mater., 2012, 24, 663-668.

(92) Wen, Z.; Ma, X.; Yang, X.; Bi, P.; Niu, M.; Zhang, K.; Feng, L.; Hao, X., Chinese Chem. Lett., 2019, 30, 995-999.

Appendix

List of Figures

List of Tables

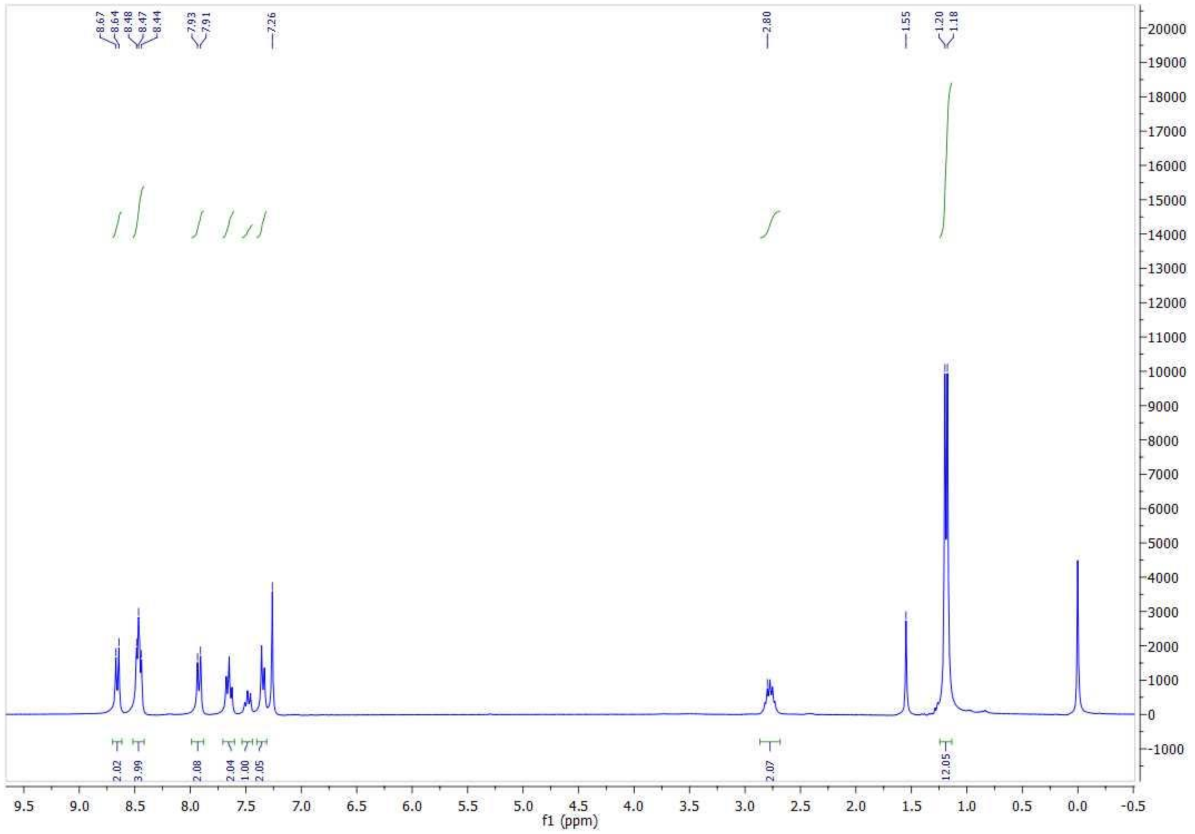

Figure 32. ^{1}H-NMR spectrum of PMI.

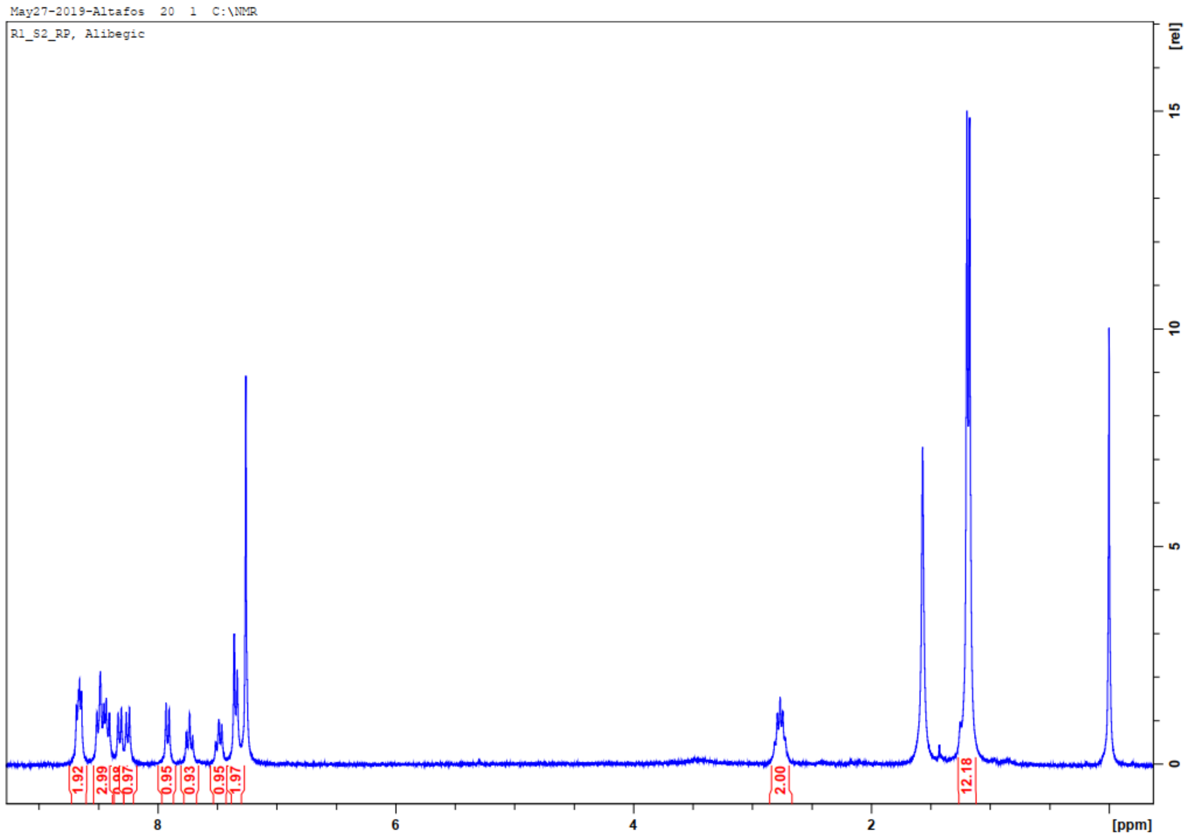

Figure 33. ^{1}H-NMR spectrum of PMI-Br.

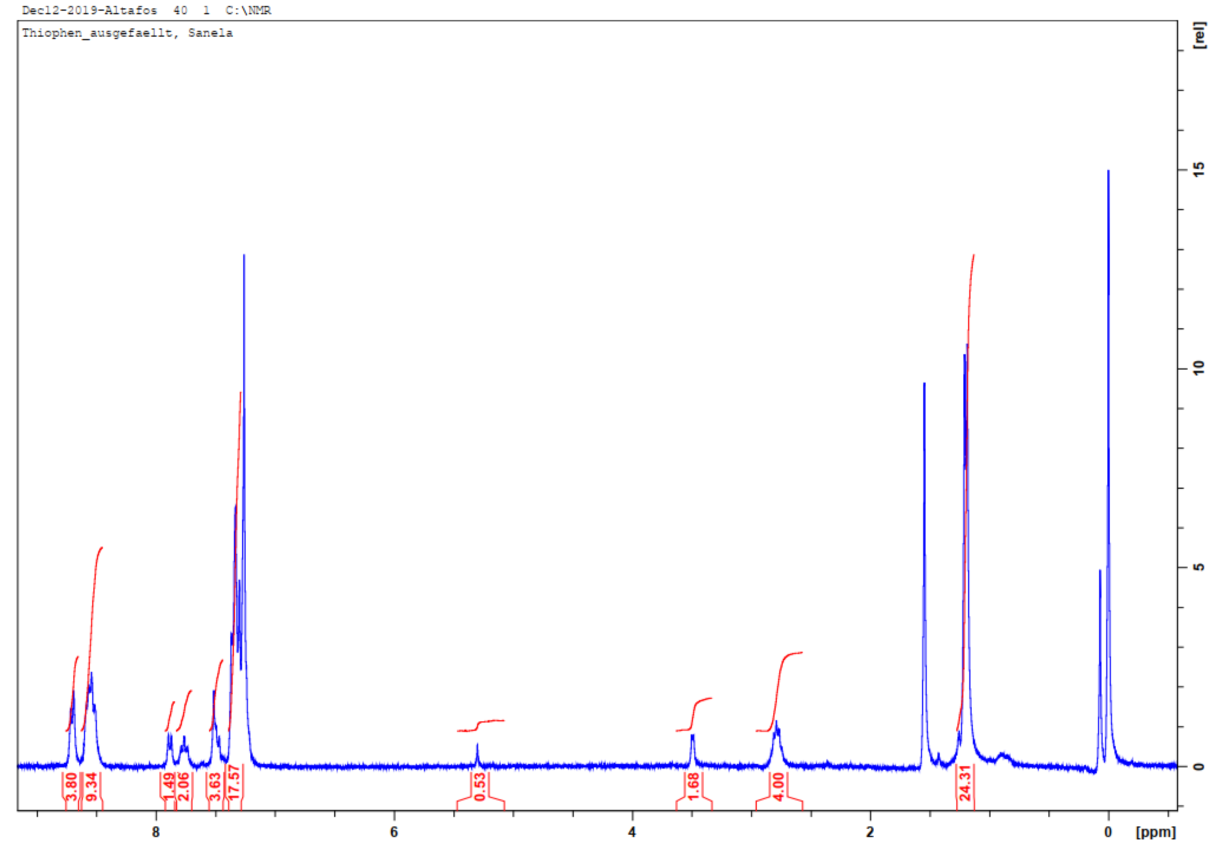

Figure 34. ^{1}H-NMR spectrum of PMI-thio-PMI.

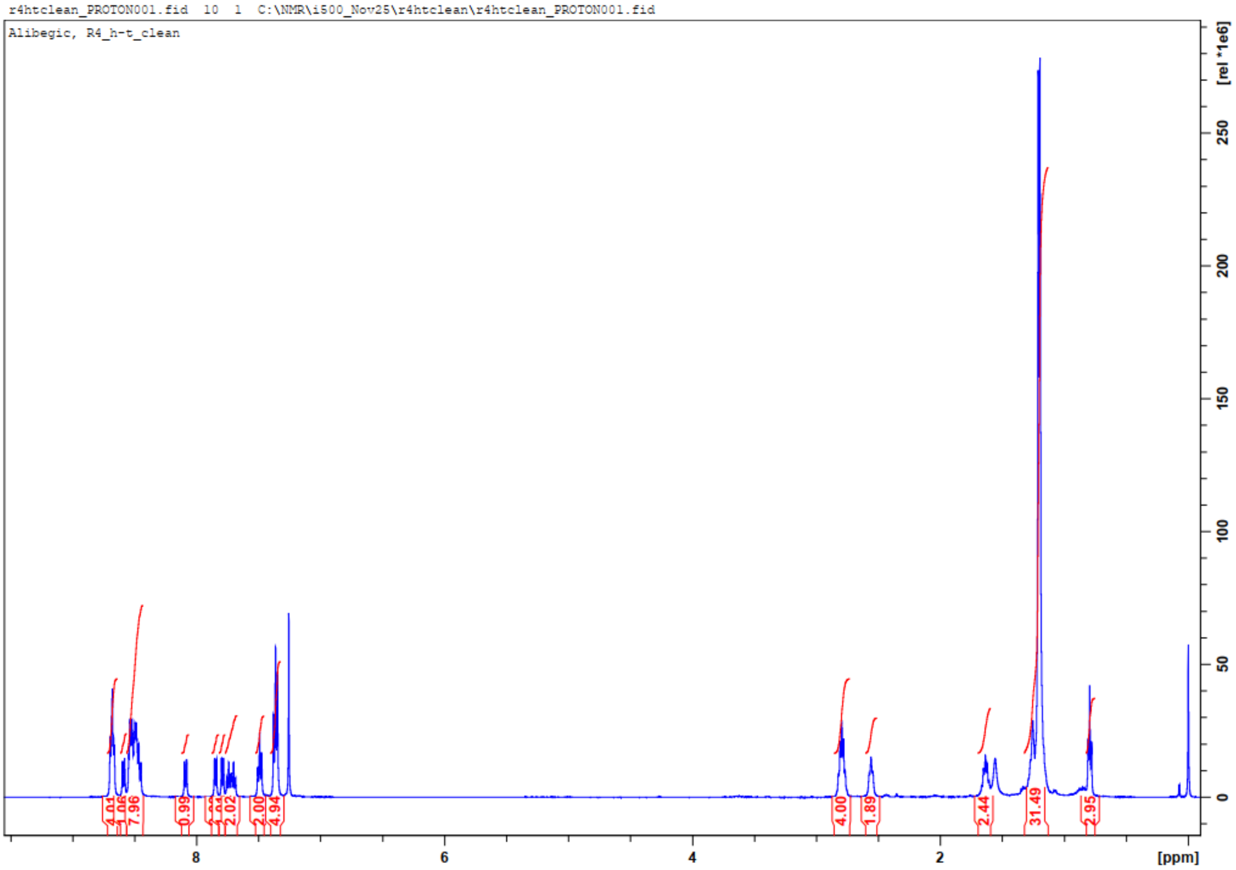

Figure 35. ^{1}H-NMR spectrum of PMI-hT-PMI.

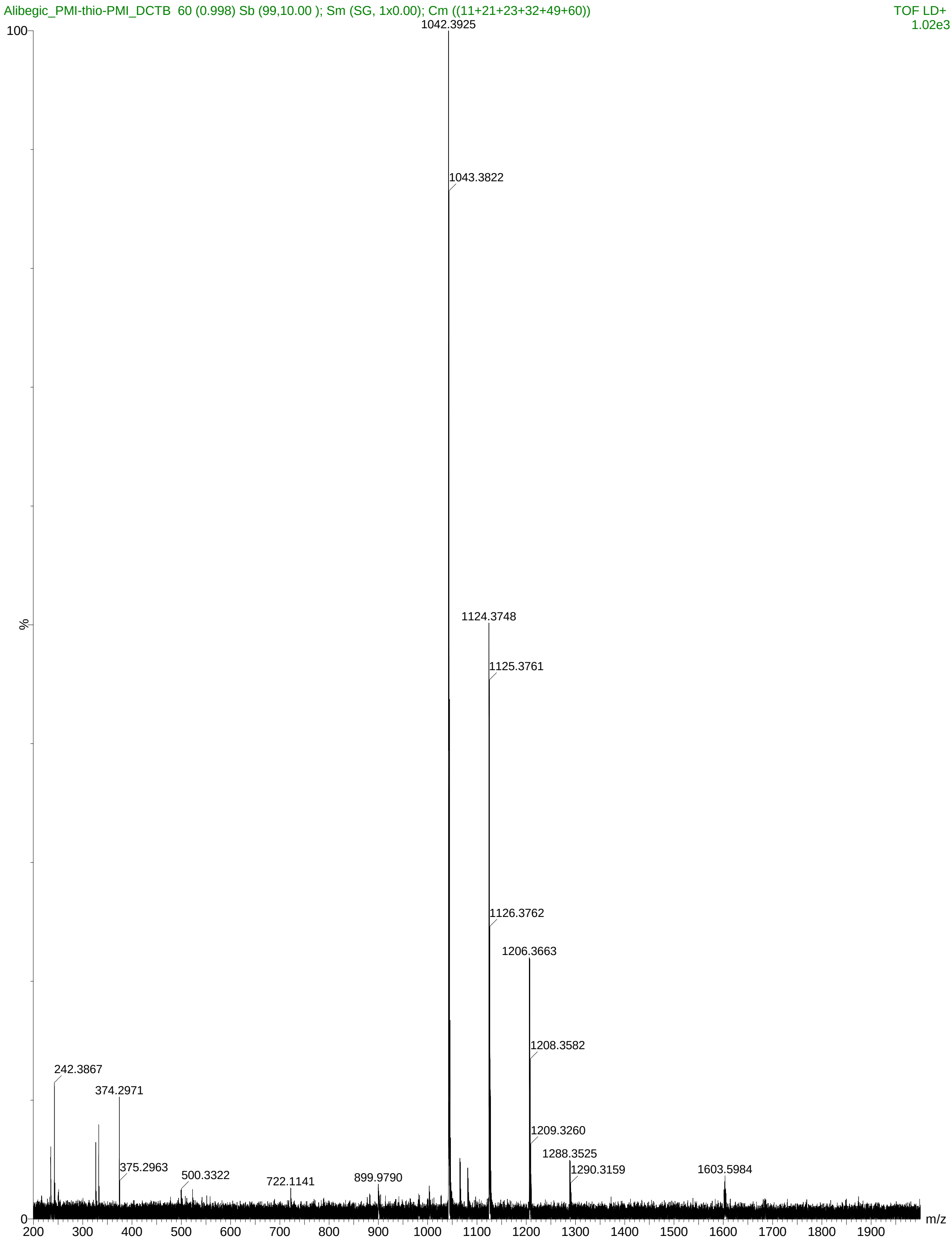

Figure 36. MS spectrum of PMI-thio-PMI.

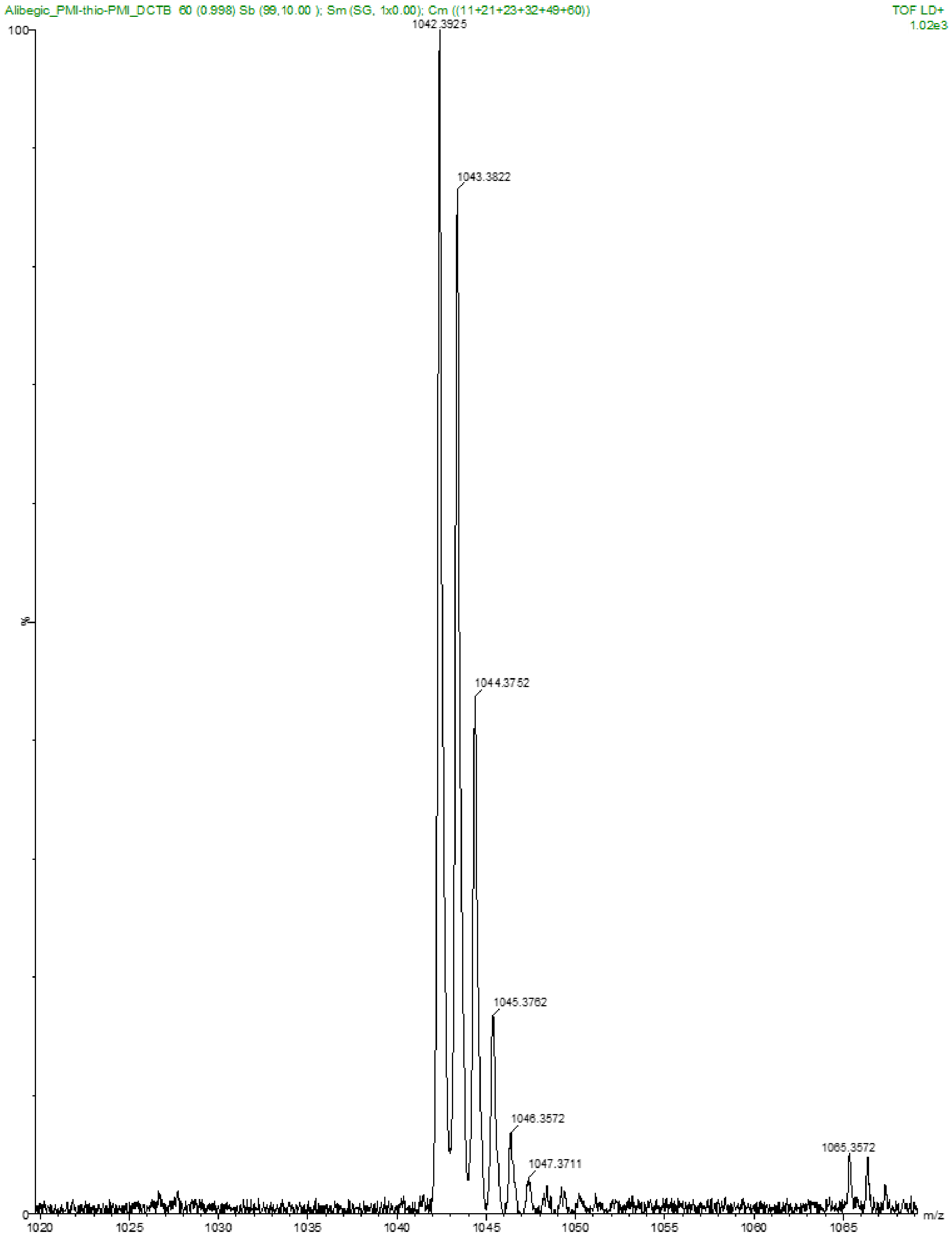

Figure 37. MS spectrum of PMI-thio-PMI.

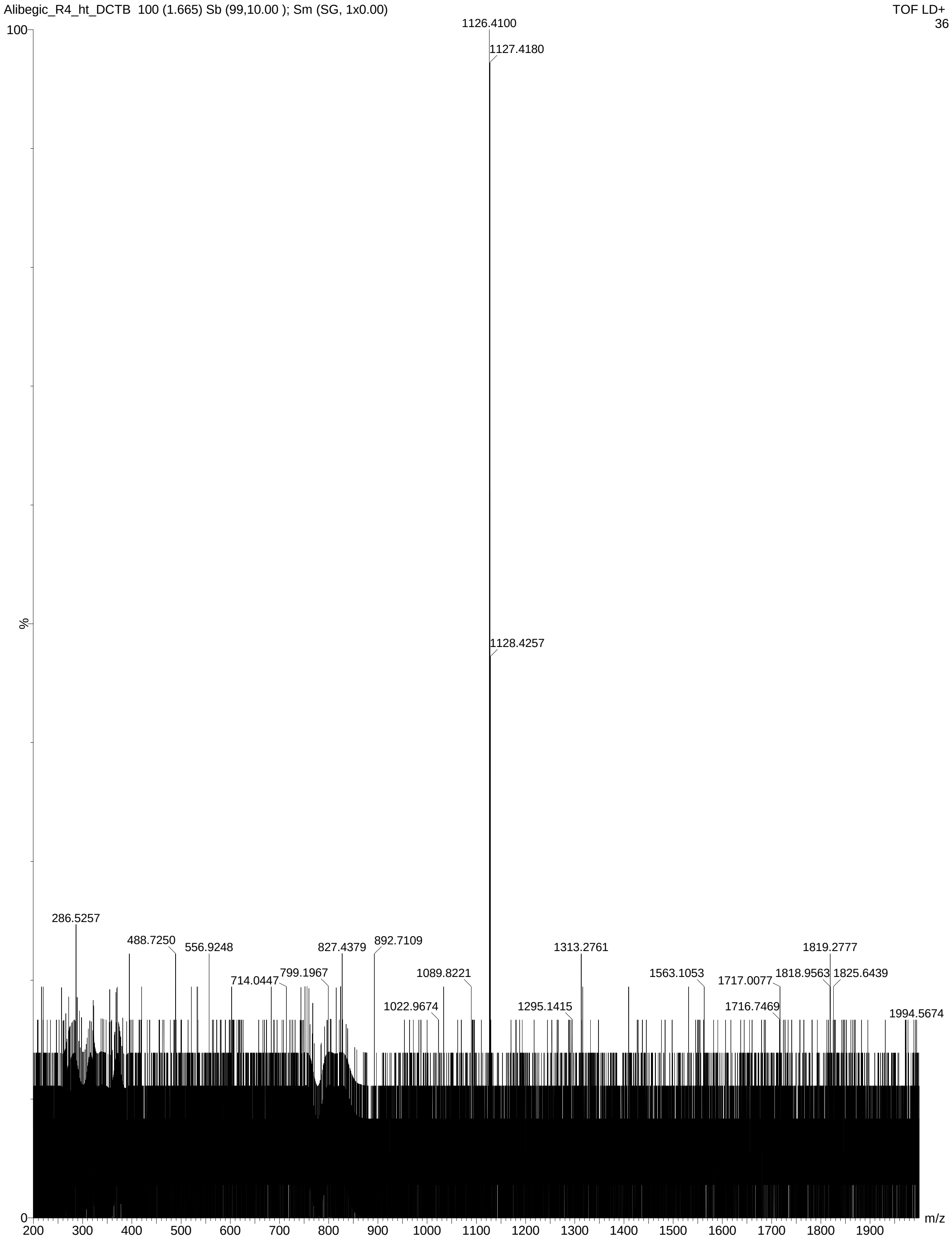

Figure 38. MS spectrum of PMI-hT-PMI.

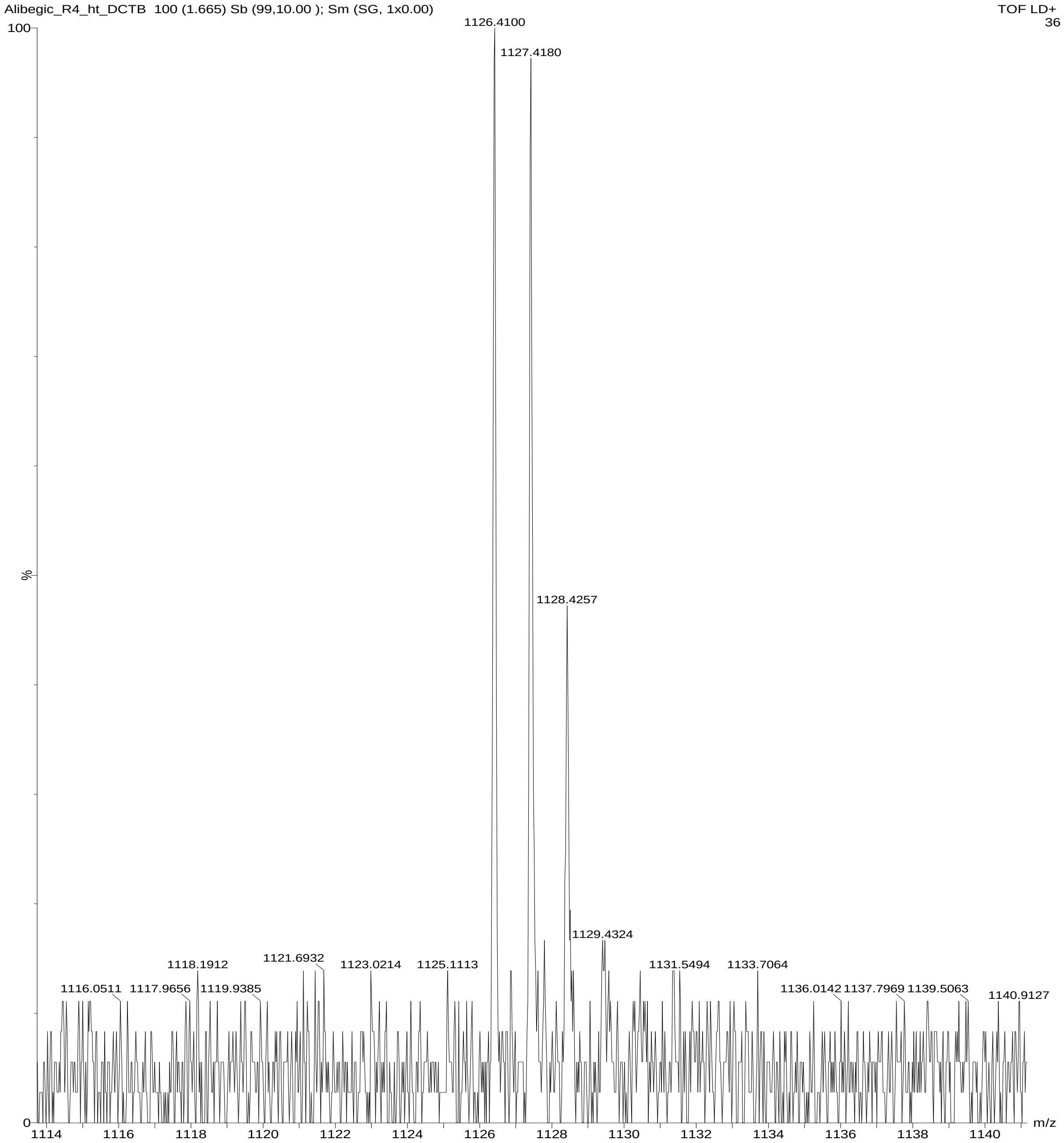

Figure 39. MS spectrum of PMI-hT-PMI.